PRACTICAL DESIGN OF A HIGH-VOLTAGE PULSED POWER SUPPLY FOR

DOWNHOLE PLASMA ENHANCED GEOTHERMAL DRILLING

A Thesis

by

FNU SANAT KUMAR

Submitted to the Office of Graduate and Professional Studies of
Texas A&M University
in partial fulfillment of the requirements for the degree of

MASTER OF SCIENCE

Chair of Committee,	Dion S. Antao
Committee Members,	David Staack
	Sam Noynaert
Head of Department,	Bryan Rasmussen

May 2021

Major Subject: Mechanical Engineering

ABSTRACT

Energy demand worldwide has grown by 14% over the last decade driven by increasing industrialization and stronger heating and cooling needs in some regions. At a time when society is becoming increasingly aware of the declining reserves of fossil fuels along with environmental issues such as fossil-fuel-sourced greenhouse gas (GHG) emissions, use of renewable and sustainable energy sources is the appropriate and applicable choice. Geothermal energy is one form of a sustainable source, which has certain advantages that make it a viable solution for helping meet the world's energy needs. Geothermal drilling is done most often through hard rocks rather than through the softer, sedimentary rocks of petroleum-bearing formations. The harder rock lithology decreases the rate at which drilling occurs and increases the wear and tear on drilling tools. These factors add up to significant time and money expenditure. In order to make geothermal drilling more efficient and cost-effective, new technologies need to be developed.

We focus on a novel geothermal drilling technology where we weaken the rock formation before the drill bit makes contact with it by locally directing high energy shockwaves at the rock formation using electrically induced microsecond plasma discharges in liquids. The shockwave results in microscale fractures in the rock formation, and the resulting lower compressive strength lithology is easier to drill.

To generate the microsecond high energy pulsed plasma discharge, our concept uses existing components of a drilling bottom hole assembly (BHA) such as the mud motor and

alternator to generate power in situ. This thesis focuses on the design, assembly and characterization of the major electrical circuit required to generate the electrically induced microsecond high energy plasma discharge. Finally we designed a bottom hole assembly where the proposed plasma enhanced rock reduction may be used and we characterized the performance of an 80 J per pulse rectification Cockcroft Walton generator (CWG) circuit at atmospheric pressure and room temperature (at different input ac power frequencies).

DEDICATION

I would like to dedicate this thesis to my mother, father and friends for their endearing

support.

ACKNOWLEDGEMENTS

Finally, thanks to my mother and father for their encouragement and support.

TABLE OF CONTENTS

LIST OF FIGURES

LIST OF TABLES

1. INTRODUCTION

1.1. Renewable Energy

The depletion of fossil fuels and environmental problems such as pollution has encouraged the search for alternatives to non-renewable energy sources such as diesel, gas, etc. which play a vital role in the industrial, residential, and transportation sectors globally. According to a report published by BP less than 60 years is the estimated time for global fossil fuel extraction without a considerable discovery of oil and gas reserves in the near future [1]. Burning of non-renewable energy sources (e.g. coal, petroleum, and oil) results in the emission of heat-trapping gases that are released into the atmosphere such as carbon dioxide (CO_2) and methane. As compared to the 20th century average of 13.9 °C (59.0 °F) [47] the global average temperature had increased by 0.69 °C (1.24 °F) as of 2014. The global temperature is expected to continue increasing unless drastic measures are not taken. Research on climate change was started in the late 19th century [2], but it was not until recently that the general public, national governments, and the energy sector started initiatives to alleviate its effect/progress [3]. In order to encourage citizen-level effort to use alternative energy sources and individual consciousness of energy use, different initiatives such as carbon taxes and new fuel economy standards have been introduced [4,5].

Reduction in emissions will occur when there is a shift in energy dependency from fossil fuels to renewable sources which has greatly reduced greenhouse emission (Figure 1.1). There are various renewable energy sources such as wind, solar, hydro, nuclear, etc.

to produce electricity. There are many non-idealities associated with these resources e.g., for wind and solar fluctuate throughout the day/ season/ year, and nuclear waste disposal is challenging. Geothermal energy is a resource that does not have these concerns. It is one of the sources where the operator of a geothermal energy facility can control the rate at which heat is extracted because the geothermal heat flux does not vary, providing flexibility in energy supply that can match the oscillations in energy demand [48].
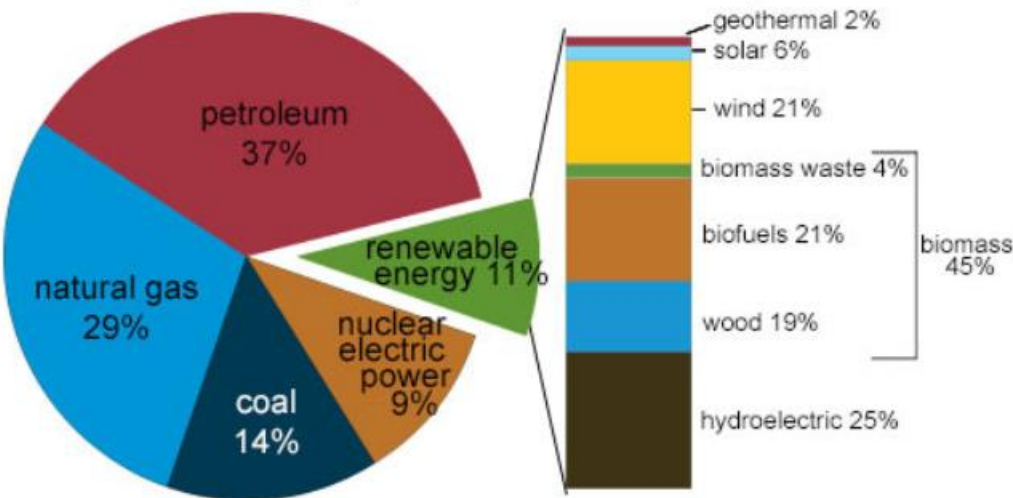
Figure 1.1 US energy consumption by energy source for the year 2017 [49]

1.2. Geothermal Energy

The word geothermal is derived from two Greek words – therme and geo [6] which mean the heat and earth respectively. Thus, the meaning of geothermal energy is heat from within the earth. Because geothermal energy is obtained from sources that are inexhaustible, it is classified as a renewable energy resource. The earth's core lies about

2

4,000 miles [6] under the earth's surface (see, Figure 1.2), which has two layers, molten iron surrounding a solid iron center. The temperature of this core is estimated to be 2800 ≈ 6000 °C [7]. The earth's core is surrounded by 1,800 miles thick mantle. It is partly rock and partly magma. The outermost layer of the earth is like an eggshell, which is an insulated crust and has some broken pieces. These broken pieces are known as plates. The source of this energy is the molten metal within the earth's core and the steady exothermic decay of radioactive material because of which there is a constant heat flux moving through the earth, making geothermal energy a renewable resource [48,50]. As such, the temperature of the ground increases as you move deeper into the earth. Conventional hydrothermal energy systems use water in liquid or vapor form to extract heat from faults and fractures. Geothermal energy can be used for multiple applications under the appropriate conditions. Such conditions are commonly found near volcanic activity, tectonic plate boundaries, or hot spot anomalies [7,51]. Thus, re-usable thermal energy can be harvested from the earth.
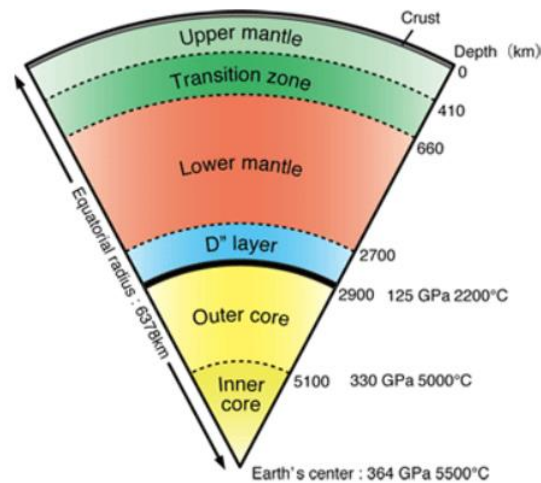
Figure 1.2 Layered structure of Earth's interior along with pressures and temperatures [52]

This thermal energy, which is known as geothermal energy, can be found anywhere on earth and can be used in many ways. It is used to produce electricity, heat buildings, and greenhouses, among other uses. This energy can be produced 24 hours a day and at a large scale without emitting greenhouse gases. This makes it a sustainable solution which reduces the dependence on fossil fuels and helps with global warming concerns.

1.3. Drilling Operation

In order to reach energy sources within the earth such as oil, natural gas, or geothermal, we have to drill to the depth within the earth where the resources can be harvested. This action can be performed with simple tools if time is not a concern; however, to most companies, the faster you can procure these resources, the more profitable it is. Improvements to the drilling process are always of interest to drilling

companies. A general drilling operation involves a drill rig above ground with electrical generators, mud pumps, mud pits, water storage, control systems, and tools to add/remove piping from the drill string, and extract and transport the resources from the well. The drill string consists of all the components that enter the well: piping, string stabilizers, safety catches, drill collars, heavyweight piping, joints, couplings, bearings, a mud motor, and a drill bit.

One can argue that the drill bit is the most important feature in the string because it is what actually drills the well. The bit must be able to drill through many different rock formations, some with extremely high compressive strength (>100 MPa or >15 ksi [8, 9]), such as crystalline rock, while under thermally challenging environments (>200 °C [9]), and with downhole equipment exposed to corrosive environments [10, 11]. Typical drill bits used are roller-cone and drag bits with polycrystalline diamond compact (PDC) inserts; however, high temperature and corrosive environments favor drag bit type drills due to the absence of moving parts (i.e., no bearings, seals, and lubricants) [11]. This leads to significant wear to the drill bit, with the harder rocks leading to faster wear, and more maintenance needed. Down-time or Non-Drilling Time (NDT) adds to the drilling costs in addition to maintenance and operating costs, so any methods to minimize these impacts are highly sought after.

It has been observed that "pre-fracturing" or "altering" the rock prior to drilling has a large impact on increasing the ROP as the effective strength of the rock is reduced [10, 12]. A number of enhancement technologies have been proposed including chemical enhanced drilling (CED), jet-assisted drilling (JAD), and laser enhanced drilling (LED).

However, there are key concerns with respect to operational difficulties including safety, operational sustainability, and feasibility. While "pre-fracturing" or "altering" rock prior to drilling is effective in increasing ROP, uncontrolled damage of the rock can lead to poor borehole quality, loss of circulation, and ultimately increased NDT [11].

1.4. Thesis Overview

With the energy industry as competitive as ever, companies are interested in accessing energy resources faster. Current methods for drilling wells involve the use of long drill strings that drill deep into the earth to reach these trapped resources of energy. Drill strings have numerous parts that wear with time of use, especially the drill bit. The drill bit is exposed to hard rock formation and the wear and tear require maintenance and or replacement.

The concept in focus in this study adapts the drill string to allow the drill bit to do less work, by weakening the rock formation before the drill bit makes contact with it. This is done by emitting a high energy plasma at the tip of the drill bit, directed towards the rock formation. The plasma and subsequent cavitation phenomena cause microfractures in the formation and reduce the compressive strength that the bit has to overcome. Less work for the bit results in less downtime for maintenance and bit replacements, as well as an increased Rate of Penetration (ROP).

To power the high energy, and ultrashort timescale ($\approx 10\mu s$) plasma the concept uses the existing drilling fluid/mud and mud motor to generate power. The power is upconverted to ultrafast time scale high energy pulses using a rectifier circuit called a Cockcroft Walton Generator (CWG). The rate of mudflow controls the power generated.

These components create a compact system to generate sufficient energy to create a plasma downhole without the need for power supplied from the surface. This thesis focuses on developing and characterizing a CWG for downhole geothermal drilling conditions.

2. BACKGROUND AND LITERATURE REVIEW

2.1. Drilling Technologies

Traditional drilling consists of many processes. (i) boring in which a drill bit and pipe are used to create a hole vertically into the ground, (ii) circulation in which drilling mud is circulated into the hole and back to the surface for various functions including the removal of rock cuttings from the hole and the maintenance of working temperatures and pressures, (iii) casing the hole in a cement casing to prevent collapse, (iv) perforations of the casing in the production zone to provide a path for the oil/gas to flow, (v) production of oil and/or gas, and (vi) abandonment of the well when it has reached the end of its useful life [14].
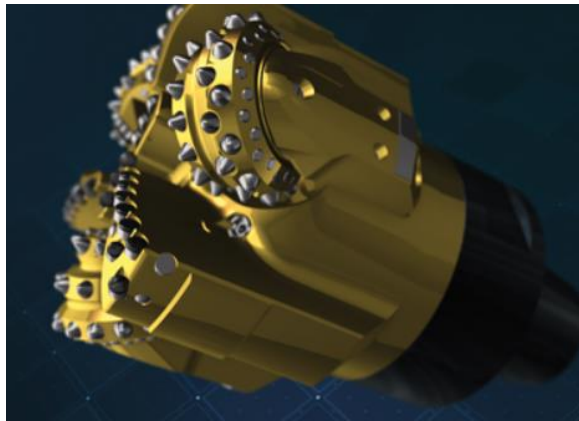
Figure 2.1 Baker Hughes' Kymera PDC roller cone hybrid drill bit [53]

2.1.1. Thermal Stress/Shock Failure Drilling

This concept uses a modified drill bit along with a downhole burner to apply a high heat flux to the rock face. The sudden temperature difference causes stress in the formation, leading to microfractures, which weakens the formation and make it easier to drill through. Stresses are introduced into the rock surface due to heating and reduce the rock strength by at least two mechanisms: (i) there are large thermal gradients between the surface and the deeper structure of the rock, which results in fragment of rock surface into small flakes called spalls, which typically have lateral dimensions several times the thickness and (ii) the different minerals which compose the rock have different coefficients of thermal expansion, so their dimensions do not change the same amount as they change temperature [41]. This method is fairly effective in High-Pressure High Temperature (HPHT) wells, such as supercritical geothermal wells, but less effective in shallower, oil/gas wells [8].

By feeding fuel and oxidizer to the burner at the lower end of the drill string energy is transferred in a thermal stress drilling system. Spalls are flushed out of the wellbore with the products of combustion from the burner and sometimes by additional air injected into the annulus above the burner [41]. For this concept, the ROP increase over traditional drilling would be minimal, depending heavily on the depth of the well. The deeper the borehole, the more efficient it would become, in theory. Because the concept is still under development, cost and energy estimates are only assumptions; however, one can presume that cost savings and energy reduction would be minimal over traditional drilling, again depending heavily on the depth of the borehole and increasing proportionally.

Table 2.1: Pros and cons of thermal stress drilling technology

Pros	Cons
Abrasive wear will be reduced since the drill pipe does not rotate	A multi-channel umbilical for fuel, oxidizer, and cooling water is required
High penetration rates in hard rock have been predicted and demonstrated	The system must (probably) operate in a gas-filled hole, limiting the application
Due to a lack of contact between the burner and the rock face burner life should be longer than the current bit life. This reduces the number of trips	Performance (ability to spall) varies significantly with rock type
	Some safety concerns, with air-fuel mixture downhole, exist
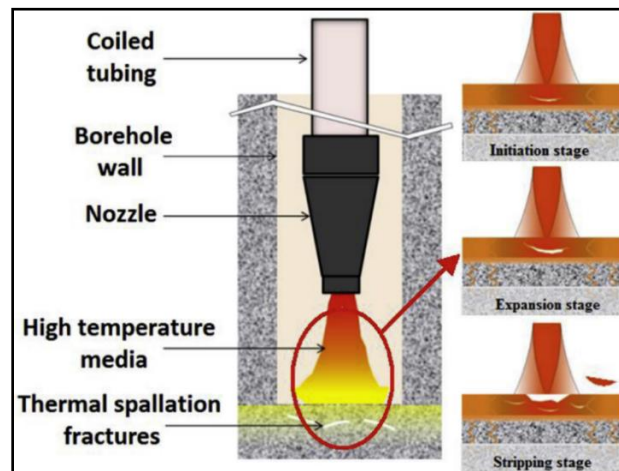
Figure 2.2 Bottom hole assembly in thermal spallation drilling and thermal spallation process [45]

2.1.2. Laserjet Drilling

Laserjet drilling (LJD) consists of weakening the rock formation through a laser beam, it reduces the wear rate of the mechanical drill bit. The laser beam can be modified and guided using optics to achieve specific beam diameter and power intensity on the rock. Depending on the optical properties of the rock, a fraction of the incoming laser power is absorbed and subsequently converted into thermal energy. The high-power intensity laser beam in contrast to the rock's low thermal conductivity causes the local temperature to increase rapidly, which results in the thermal stresses, and rock spallation. This weakening process in the rock due to induced thermal stresses also results in fractures, mineral dehydration, and thus, reduction in the rock's Young and shear modulus. The weakened rock may be drilled or "ground down" with reduced effort using specially optimized mechanical bit technologies. This process continues on a new surface by removing the cuttings and fragments with the help of drilling fluid as the flushing system.

The Laserjet mechanical assistance drilling system is currently being developed at the International Geothermal Centre, Bochum (Germany), and consists of two central concepts. The laser beam delivers the required thermal energy to induce spallation and rock softening and in parallel the mechanical drill bit assists in the rock breaking process. The beam hits the rock and induces the intended thermal stresses, increases the rock surface temperature to approximately 600 °C, and consequently results in thermal spallation and rock softening [10]. The major disadvantage of this concept is that, since laser beams are of smaller diameter, the holes drilled are small, and multiple beams are needed to drill multiple holes and weaken the rock formation.

(a) **(b)**
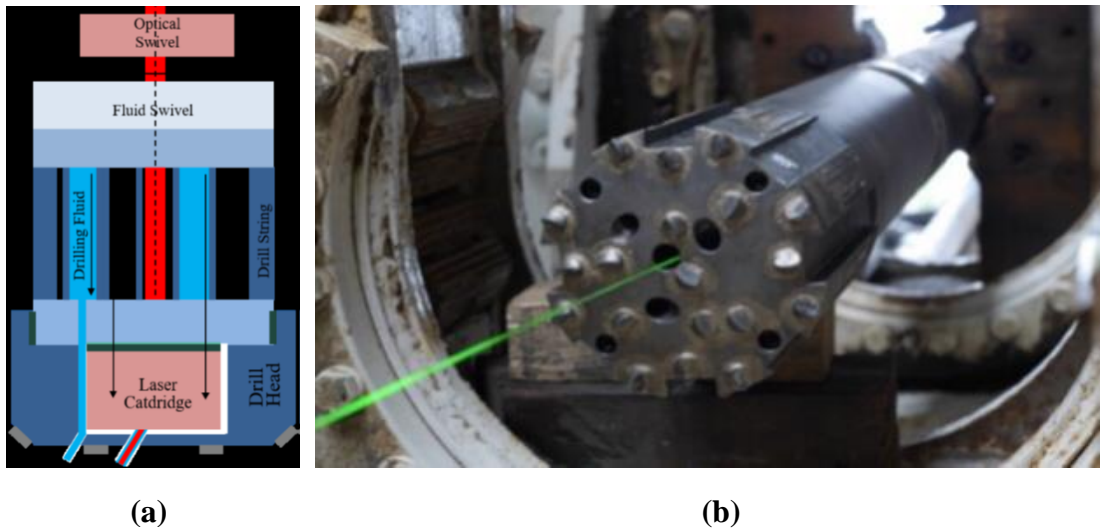
Figure 2.3 a) Schematic diagram of LaserJet arrangement inside the drill head b) Modified drill bit [10]

2.1.3. Electric Impulse Drilling

Electro Impulse Technology (EIT) uses two electrodes to create high electric voltage impulses (600 kV in 120-150 ns) that impinge on the rock and break it down. The resulting stress due to high transient voltages surpasses the dielectric strength of the rocks and damage it. In this technology, the two electrodes are required to be in loose contact with the rock and no mechanical load is required. Also, the drill head can be incorporated in a conventional drilling rig. The major components are as follows, (i) mud Motor which powers the electrical generator, (ii) electrical generator generates the required electrical energy, (iii) transformer and rectifier generate the charging voltage for the surge voltage source, (iv) surge voltage source generates high voltage impulses, (v) trigger controls the surge voltage source, and (vi) electrodes deliver the high voltage impulses to the rocks.

This technology can be realized under downhole conditions with pressures up to 1000 bar and temperatures up to 200 °C. One of the main advantages of this technology is that it reduces the NPT (non-productive time) due to faster tool changes. Another advantage that this technology offers is the lifetime of drilling system is increased up to ≈7 times [9]. It offers several other advantages such as the extended reach of horizontal sections, better response to subsurface drilling conditions without changing the operations of the drill rig, and reduced impact on the environment.
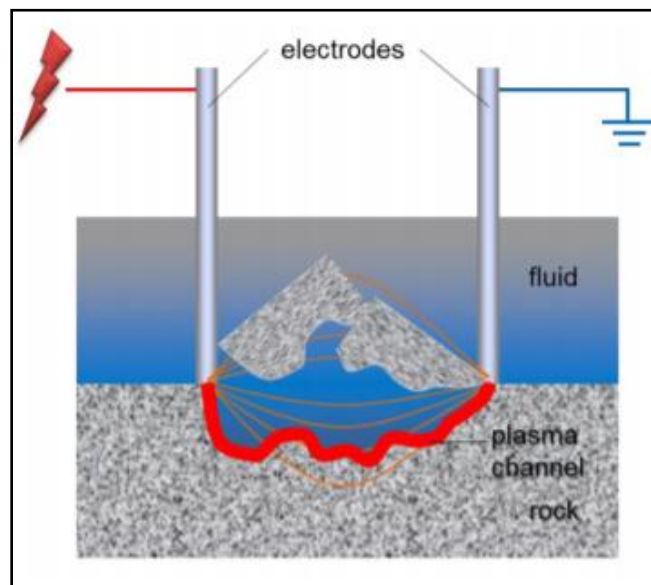
Figure 2.4 Scheme of Electric Impulse drilling [44]

2.1.4. Percussion Drilling

Percussion drilling is a down hole drilling method, in which rock reduction is achieved by alternatively lifting and dropping a heavy cutting or hammering bit that is

attached to a rope/cable that is lowered into an open hole or inside a temporary casing. In rotary percussion drilling, a variety of roller bits mounted at the end of a rotating string of rods break the rock. This is followed by a hammer action to penetrate hard material. Rotary percussion drilling has widely been recognized for its potential to drill faster, in comparison to conventional rotary drilling, where traditional roller-cone and PDC bits had been used. This ability becomes more evident when the drilling takes place in hard formations such as granites, and dolo-mites.[11]

In most cases of percussion drilling, the ROP was three times higher and the speed of drilling was increased by two-fold. However, the disadvantages of this method involve difficulties with drilling in disperse formations. Percussion drilling also faces a challenge similar to conventional drill bits, the rotary drill bit at its head undergoes wear and requires frequent replacement, causing an increase in down time and cost [12].

Figure 2.5 Solid-head bits for percussion drilling [11]

2.1.5. Hammer Drilling

Hammer drilling uses fluid to power downhole hammers during the drilling process. In this concept instead of depending on the weight of drill collars to load the rock in compression a reciprocating piston applies an impulse to the bit. Hammers can be used on either solid-head bits with tungsten-carbide inserts or conventional roller cone bits. This concept gives high rates of penetration at shallow depths where little drill collar weight could be carried and in brittle rock as compared to the traditional drilling system because of the hammer's high-frequency impulses, coupled with the lack of fluid-column pressure. Downhole hammers are relatively inexpensive to use but require a fluid drilling scenario, need precise weight-on-bit control, and often suffer severe gauge wear with solid-head bits [42]. Some of the positive and negative features of this system include the following:

Table 2.2: Pros and cons of hammer drilling technology

Pros	Cons
Lower weight-on-bit gives longer bit life	Fatigue may cause mechanical failure of the valve and/or spring
Penetration rate increases with more effective rock reduction	Abrasives in mud cause erosion and wear at the control valve
Fluid hammer requires little modification to standard drilling practice (possible -	Performance improvement decreases with depth

15

Table 2.2: Continued

Pros	Cons
addition of a shock-absorber above the hammer)	
Lower WOB gives less tendency for hole deviation	Hammer interferes with mud-pulse or acoustic MWD
	Poor design or incorrect operation can cause excessive damage at the hammer-anvil interface
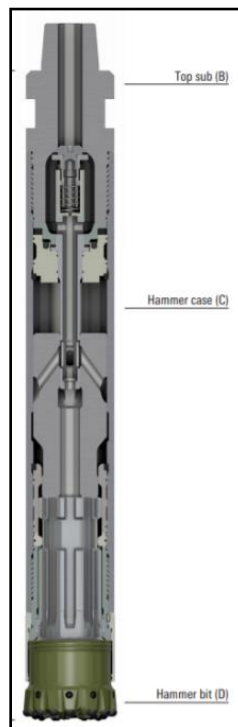
Figure 2.6 Impax hammer system [54]

2.1.6. Plasma Drilling

Plasma drilling is a method of drilling based on the use of a plasma drill or specially designed plasmatron. The temperature of the plasma jet in plasma drilling may be as high as 5000 K, which is sufficient for the destruction of rocks at the bottom of the hole. The plasma-forming materials in plasma drills are air, inert gases, water vapor, and mixtures thereof.

The principle of operation of a simple air plasma drill is as follows. Compressed air is supplied through a hollow drill rod to the plasma drill, where it is separated into two streams. One stream proceeds to the internal electrode through a spiral swirling channel, feeds the discharge, and by blowing on the arc forces it to rotate. The rotation displaces the electrode spots of the arc over the surface in the interior of the electrode and thereby prevents the premature burning out of the electrode. The second stream cools both electrodes by flowing around their cooling fins. A part of the second stream proceeds through tangential openings in the insulating sleeve into the discharge chamber. The plasma that has been formed flows out through one or more nozzles toward the bottom of the drill hole. After the cooling of the electrodes, a large part of the second stream is ejected to the outside through openings in the plasma drill cover and carries the drilling debris out of the drill hole [13].
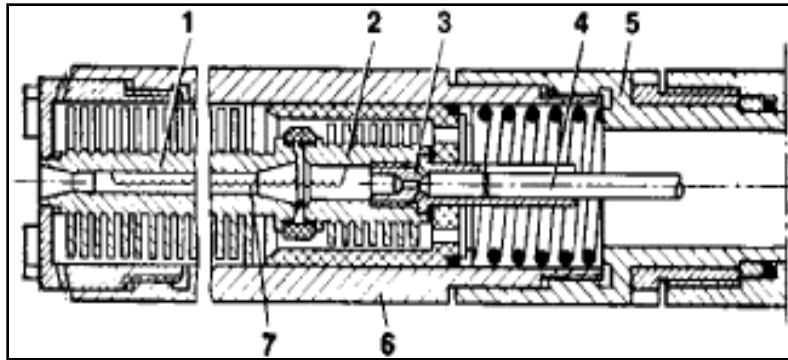
Figure 2.7 Air-cooled plasma drill: (1) output electrode, (2) internal electrode, (3) swirl cone, (4) stem, (5) drill rod, (6) casing, (7) arc [13]

2.1.7. Shock and Plasma Accelerated Rock Cracking (SPARC)

This concept (SPARC) is inspired by the snapping shrimp tunneling activity in limestone or basalt [20] using cavitation [21-23]. In SPARC, an electric discharge using high energy pulses is produced which induces micro-cracks on the rock surface. The discharge is generated underwater and the energy deposited into the plasma channel results in a sudden increase of pressure which expands and collapses as a cavitation bubble accompanied by shock waves and mechanical stress waves. These pressure waves with the pressure exceeding 1 Gpa [24-27] lead to micro-cracks on the rock surface. The hypothesis is that micro-cracks on the rock surface lead to a reduction in the cutting energy as well as an increase in the amount of material removed for the same cutting process. This would be due to an increased frequency of chipping and the smaller size of chips as the rocks are pre-cracked. The key factor for this technology is the ability to generate localized power for the plasma pulses downhole and in a drill string form factor. This downhole energy conversion unit/process is the focus of this thesis study.

18

3. SHOCK AND PLASMA ACCELERATED ROCK CRACKING (SPARC)

3.1. Bottom Hole Assembly Design

We have designed one possible embodiment of the bottom hole assembly (BHA, Figure 3.1) where the novel SPARC technology may be leveraged. In this technology high energy pulses induce cracks on the rock surface due to the sudden increase of pressure (shock waves) and mechanical stress waves which results in the reduction of cutting energy as well as an increase in the amount of material removed [63]. We have designed this setup to generate high energy pulses from drilling mud in a downhole environment. The up-hole components of the BHA are similar to any commercial drilling technology where a mud motor (positive displacement unit) uses the flowing drilling fluid to rotate the drill head. The mud motor, constant velocity (CV), bend and bearing assembly sections/components are common in existing commercial technology. The novelty in the design lies down-hole of the bearing assembly. An alternator connected to the mud motor is used to charge a battery bank. The battery bank provides power to an inverter and transformer to convert low voltage ($\approx$48 V) dc electrical energy to the high voltage ($\approx$10 kV) ac input required by the step up and rectification module. The transformer is connected to a high voltage ac-to-dc rectification and amplification circuit (the Cockcroft Walton generator or CWG) since high voltage dc is required at the electrodes to generate the plasma discharges during drilling. Between the CWG and the electrode pairs embedded within the drill head/bit, we have a distributor head (multiple spark gaps) which will provide appropriate timing for the generation of plasma discharges at the desired

19

electrode pair and depending on the electrode position spatially on the drill head cross-section. Figure 3.2 shows a schematic flow/block diagram of the bottom hole assembly integrated with the existing drilling components. This BHA embodiment will be connected to commercially available drilling components at the bearing assembly and before the modified drill bit (drill bit with embedded electrode pairs). The drilling mud will flow through the outer section till the bend assembly and enter the inner section of the bend assembly. The drilling mud will exit through the nozzle on the drill bit similar to traditional drilling technology. The BHA is designed in such a way that it integrates with the existing drilling technology without any changes and does not hinder normal drilling operations.
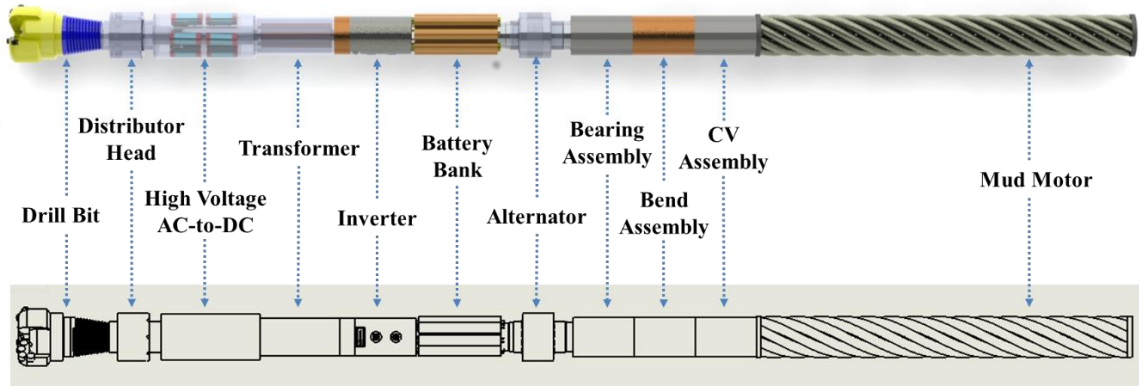
Figure 3.1 Three-dimensional rendering of the bottom hole assembly (BHA) design to leverage the plasma-enhanced rock reduction technology.
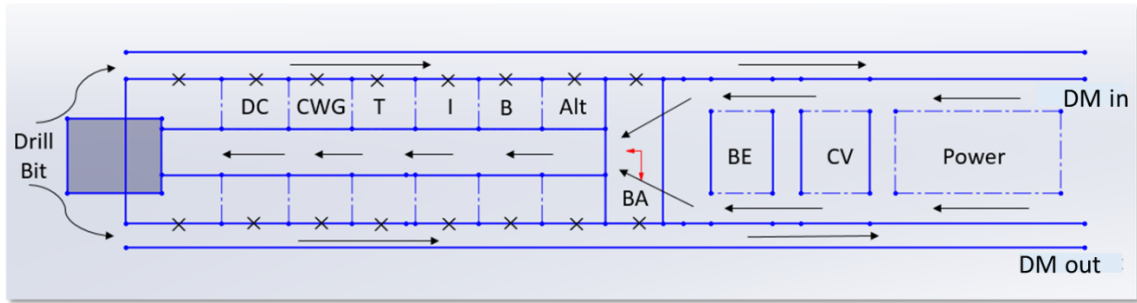
Figure 3.2 Schematic diagram for bottom hole assembly where DM(drilling mud), Power(mud motor), CV(constant velocity), BE(bending assembly), BA(bearing assembly), Alt(alternator), B(battery), I(inverter), T(transformer), CWG(Cockcroft Walton generator), DC(distributor cap)

We have also designed a drill head with integrated plasma technology [46]. Figure 3.3 shows one possible design of the drill head with electrode pairs placed on the wings. This particular iteration of the drill head consists of four electrode pairs placed at different locations. The electrodes are placed such that the discharge effects are encompassed by the entire cutting face of the drill head. This drill bit design follows API codes and the polycrystalline diamond (PDC) are 13 mm in diameter and the threaded connection is a 2-3/8 API regular pin (male) thread.
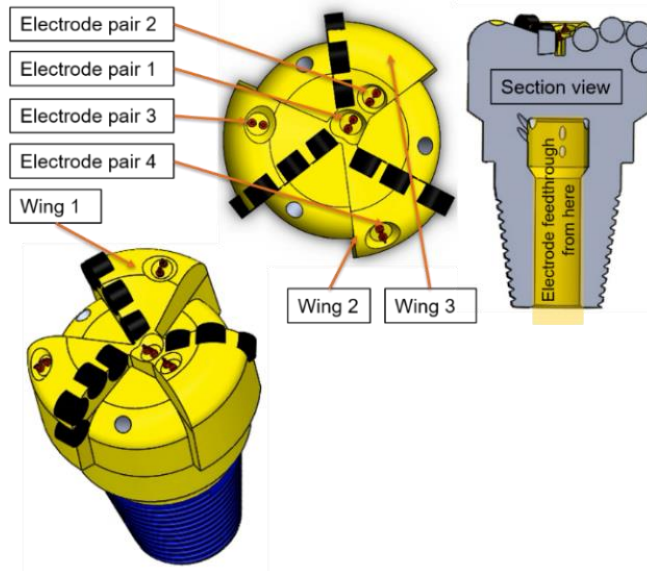
Figure 3.3 Various electrode pairs shown in the 3D CAD design with wire channels running through the section view [46]

3.2. Component Selection for the SPARC Bottom Hole Assembly

In this section we present the various BHA components which would be ideal for the SPARC technology in terms of form-factor and specifications. All components discussed in this section apart from CWG and distributor are available off the shelf and are currently used in the oil and gas/geothermal drilling industries. The major requirement for our BHA assembly is to convert hydraulic energy (flowing drilling mud) to electrical energy (40 kV and 80 J/pulse plasma discharge) and all component specifications are based on this requirement.

3.2.1. Alternator

The 22WP6 Ducommun alternator [37] is the best match for our requirements (48 V dc output), it provides a minimum RMS voltage of 19 V and is able to function at various

rpm upto 1000. The 22WP6 series alternator operates at high temperature/high pressure (HTHP) of 232 °C (450 °F) and 2068 bar (30,000 psi). It has a 2.2" outer diameter which meets our form factor requirements as shown in Figure 3.**4**.

Figure 3.4 **Ducommun's permanent magnet alternators for downhole exploration [37]**

3.2.2. Battery Bank

The Sharewell battery bank[38] with 29 V battery voltage (single battery), battery capacity ≈ 34-42 Ah, and an operating temperature of 180 °C is optimal for our needs (48 V dc). The battery bank would require a total of 2 battery modes connected in series to get a total voltage higher than 48 V. This battery bank is capable of operating at elevated pressure and has a diameter of 1.485" and length of 61.9" which is shown in Figure 3.5.
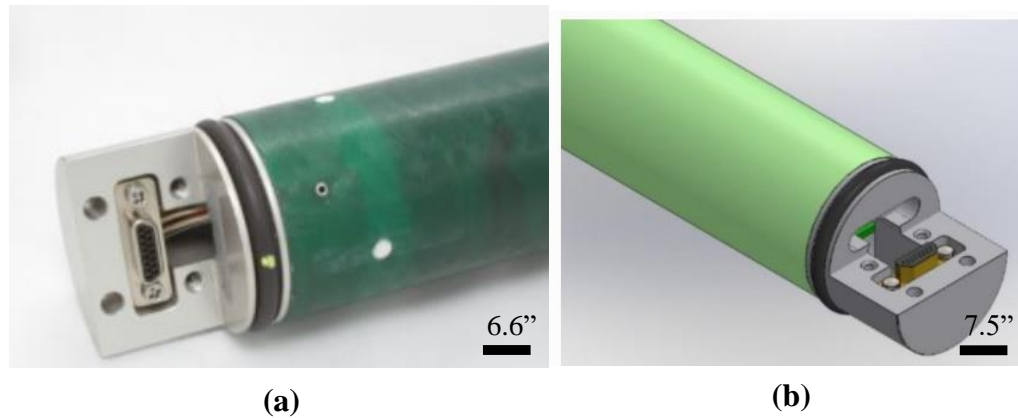
Figure 3.5 Sharewell high-temperature applications batteries: (a) Physical model of the battery, (b) CAD Model (top view) [38]

3.2.3. Inverter

The Arkansas power electronics international Inc inverter [39] is made from silicon carbide (SiC) which can withstand the high temperatures (operating temperature limits for SiC can exceed 600 °C) experienced downhole and is suitable for our application (120 V ac). Silicon carbide architectures also benefit from its high thermal conductivity [58]. Finally, silicon carbide architectures can be scaled down by 50% or more depending on the application. Figure 3.6 shows a high temperature silicon carbide inverter from Arkansas power electronics Inc.
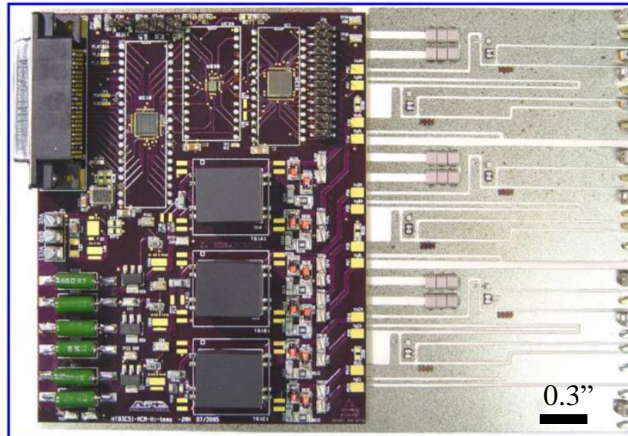
Figure 3.6 High-temperature inverter [39]

3.2.4. Transformer

A custom-made step-up cylindrical transformer may be used whose input ac voltage (primary coil voltage) is 120 V and the output ac voltage (secondary coil voltage) is 10 kV as shown in Figure 3.7. All the components of the transformer will be rated for high temperature operation. The dimensions of the transformer will be used according to the downhole form factor required. It can also be made curved to fit within an annulus. Proper insulation will be provided so that the system can handle high temperature and pressure [40].
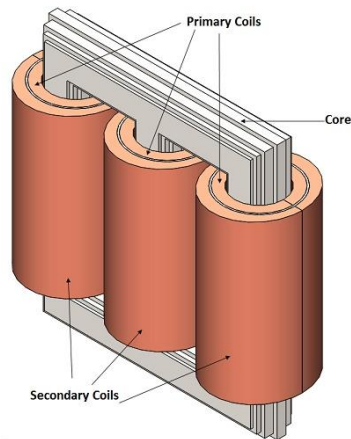
Figure 3.7 Schematic diagram of a cylindrical transformer

3.2.5. Cockcroft-Walton Generator (CWG)

A CWG is a circuit that generates high voltage dc from either a lower voltage ac or a pulsing dc input. It is a network of capacitors and diodes as discussed later. The voltage across each stage of the circuit is equal to twice the peak (or amplitude) input voltage of a half-wave rectifier. This high voltage multiplier design offers better circuit durability and long-term operation robustness, but still delivers the same required breakdown voltage, plasma energy, and power consumption.

3.2.6. Distributor

The role of the distributor is to route high voltage from the CWG to different electrodes in a specified sequence, and with appropriate timing. As the rotor rotates within the distributor, the current is able to jump small air gaps between the source (CWG) and the load (electrodes).

3.2.7. Electrodes

Tungsten electrodes will be used in this application. Tungsten is high-temperature compatible which is essential for this SPARC application.

3.3. CWG Design Setup

In this section we present the Cockcroft Walton generator circuit, describe different components of the circuit, discuss the design of the CWG circuit in a downhole form factor and discuss the different factors which affect CWG design for this downhole application. The major requirement for our CWG circuit is to provide plasma pulses of 40 kV and 80 J. The number of electrodes on the drill bit and the drill bit RPM will determine the frequency of the plasma discharges and the total energy requirement of the circuit.

The first CWG circuit was used by Cockcroft and Walton in their proton accelerator [31] and after that initial use various improved circuits were developed to power CW-type accelerators. Henneberke made a 7-stage CWG power supply with 1.5 MV and 3 mA output [32]. Reginato and Smith constructed a 600 kV and 10 mA CW power supply (18-stage) driven by a 100 kHz oscillator [33]. Hara constructed a 3-stage 200 kV/200 mA output symmetrical Cockcroft-Walton (SCW) circuit using a 1 kHz power source [34]. Joseph et al. [35] discussed operation of multiplier circuits such as half-wave voltage doublers and tripler circuit, and the guidelines for electronic components selection for diodes and capacitors. Spencer et al. (2001) [36] designed a prototype surface mounted Cockcroft-Walton board and tested for use in a battery-operated, palm-sized radiation detection device and it provided an output voltage of 1 kV and current less than 15mA. The main advantage of using CWG as a voltage multiplier circuit compared to other

27

electrical multiplier circuits (such as the Dickson multiplier [64]) is that it eliminates the requirement for the heavy core and the bulk of insulation/potting to get high voltage at the output.

3.3.1. What is a CWG Multiplier?

A Cockcroft-Walton generator is typically used to convert lower voltage ac to high voltage dc. They are used in high voltage devices such as air ionizers, cathode-ray tubes, microwave ovens, particle accelerators, and X-ray machines. It is generally used when high voltage dc is needed but the power supply is a low voltage ac signal with low frequency ≈ 50 - 60 Hz [29-30].

Cockcroft-Walton voltage multipliers may have multiple stages based on the available input and desired output but the most basic is a single-stage voltage doubler seen in Figure 3. 8 (where (a) is a positive polarity CWG circuit, (b) is a negative polarity CWG circuit and (c) is a two stage positive polarity CWG circuit). Diode D1 is forward biased and capacitor C1 gets charged to the peak source voltage V_o when source voltage V_i is on its negative peak. There will be no voltage differential across capacitor C2 when using ideal diodes which means there will be no stored charge. On the positive half cycle, the peak voltage from the source is now in series with the voltage differential across capacitor C1, so they add together. Diode D1 is now reverse biased with a voltage difference of twice the magnitude of the peak source voltage. Diode D2 and capacitor C2 work to reduce the ripple voltage of the output waveform. Ideally, this creates a voltage differential across capacitor C2 equal to twice the amplitude of the source voltage.

This theory assumes the capacitors charge near-instantaneously and the diodes are ideal. In reality and depending on capacitor magnitude, it will take several cycles for the voltage across C2 to reach its peak at $2V_o$ (we show this later through transient circuit simulations). Additional stages can be added to create a voltage tripler, quadrupler etc. however, it is not recommended to go beyond 12 stages [28]. A higher number of stages not only slows the charge time, but it also reduces voltage regulation by increasing output ripple. Increasing the number of stages increases the output DC voltage, but it also incurs more losses, resulting in less overall power transferred to the load. The CWG design is ideal for the SPARC application because it relies only on passive components. This design eliminates the need for active switching components commonly seen in rectifiers and boost converters. The Cockcroft-Walton design also allows the input signal to act as the power supply to the entire circuit.
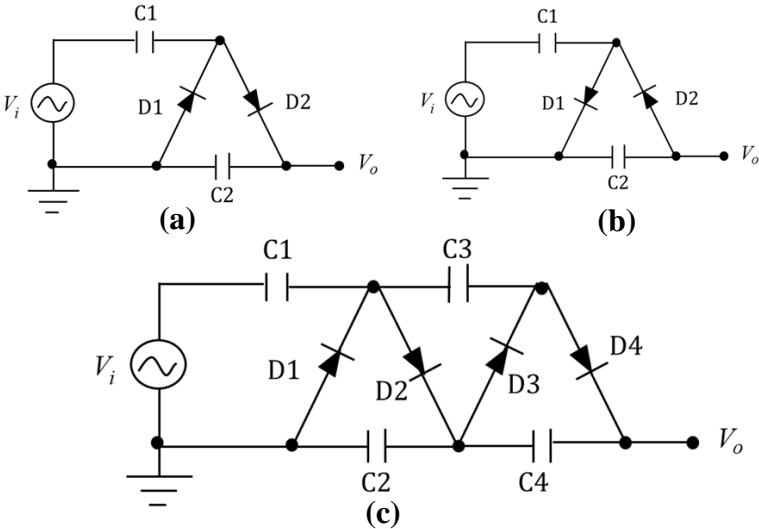
Figure 3. 8 Circuit **diagram for CWG circuit, (a) Single-stage positive polarity CWG circuit, (b) Single-stage negative polarity CWG circuit, (c) Two-stage positive polarity CWG circuit**

29

3.3.2. CWG Design in Downhole Form Factor

For the SPARC application we must design our CWG circuit in a BHA form factor. Here we designed the CWG for a 6" drill bit which uses 3-1/2" API Reg. pin connection. From the dimensions of a 3-1/2" API pipe it is clear that the maximum outer diameter of the CWG components must be 4-1/2" or less and the maximum inlet diameter would be 1-1/2" or less [59]. Based on this information we have to select circuit components such as capacitors and diodes which will fit this form factor. Table 3.1 shows four such commercially available capacitors with their dimensions, length, voltage, and capacitance value (Figure 3.9). In order to have a considerable effect on the rock surface to reduce overall energy for drilling and to increase the rate of penetration the pulse energy must be 80J. An additional requirement is that the CWG output voltage should be 40 kV. This result in the capacitance of each stage of the CWG being 100nF and a requirement for each capacitor in the circuit to handle high surge currents.

Table 3.1 Properties of different types of capacitors

Type	Figure number	Capacitance value	Diameter (inches)	Length (inches)	CWG required number of capacitors
1	Figure 3.9(a)	10 nF at 40 kV	1.35	0.55	40
2	Figure 3.9(b)	35 nF at 30 kV	1.42	5	24
3	Figure 3.9(c)	50 nF at 50 kV	2.9	16.75	8
4	Figure 3.9(d)	15 nF at 40 kV	3.3	1.2	28

(a) **(b)**

(c) **(d)**
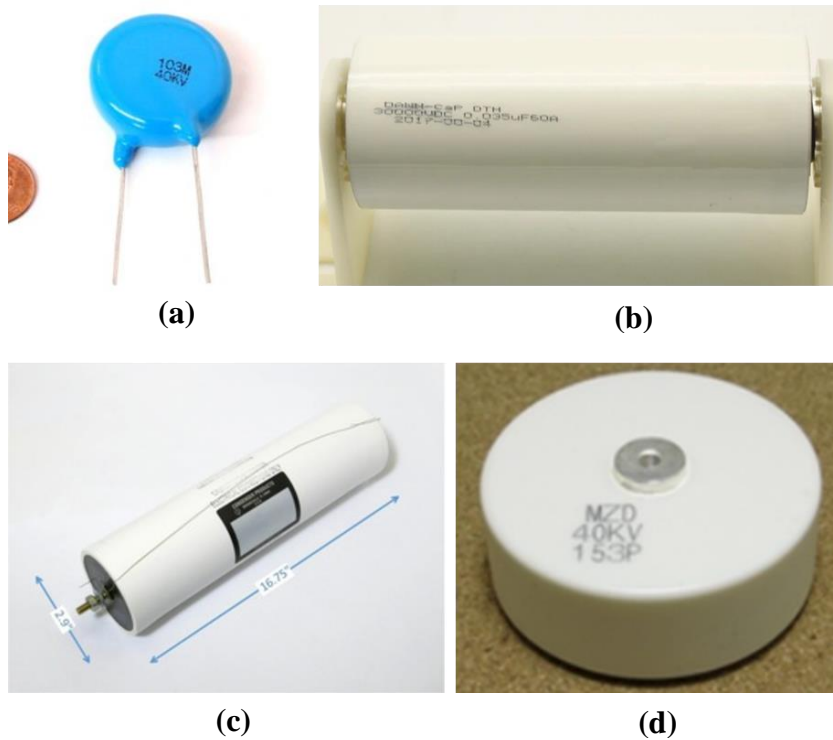
Figure 3.9 Different types of capacitors, (a) ceramic disk capacitors, (b) high voltage capacitors, (c) tesla coil capacitors, (d) ceramic doorknob capacitors

3.3.2.1. Ceramic Disk Capacitors

Type 1 capacitors which are also known as ceramic disk capacitors (Figure 3.9 (a)) are rated for 40 kV and have a capacitance of 10 nF. In order to generate 80 J, we need 40 capacitors which are connected in series and parallel (10 capacitors connected in parallel each at C1, C2, C3, and C4 in Figure 3. **8**(c)). The CAD model of the CWG circuit with this type of capacitor is shown in Figure 3.10. We ran multiple tests with these capacitors connected in our CWG circuit whose results are discussed later, however these 40 kV rated capacitors failed at output pulses of 20 kV. We hypothesize that the main reason for this may be the high surge current in the circuit during the pulsed discharges (shown in

31

transient circuit simulations). These capacitors have the most favorable sizes for our form factor, however they were not durable.
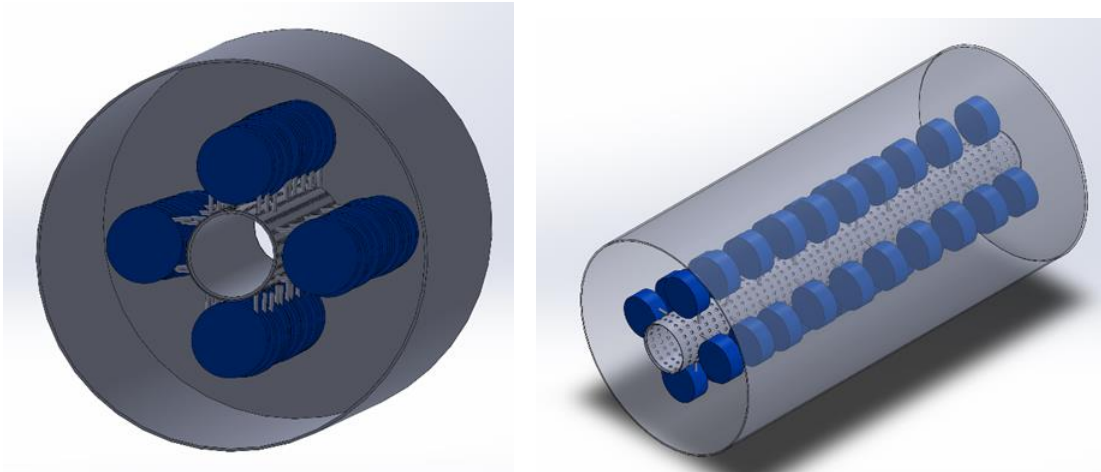
Figure 3.10 CAD model of the CWG circuit with ceramic disk capacitors

3.3.2.2. High Voltage Capacitors

Type 2 capacitors are known as high voltage capacitors and an example is shown in Figure 3.9 (b). These capacitors are rated for 30 kV and have 35 nF of capacitance. In order to generate 80 joules, we need 24 capacitors (6 capacitors connected in parallel each at C1, C2, C3, and C4 in Figure 3. **8**(c)) . We tested the capacitors in our CWG circuit, but the capacitors failed at very lower voltages (≤5 kV). Figure 3.11 shows a CAD model of the capacitor in the CWG circuit of the required BHA form factor. This design was made in the event that robust capacitors of this type become available.
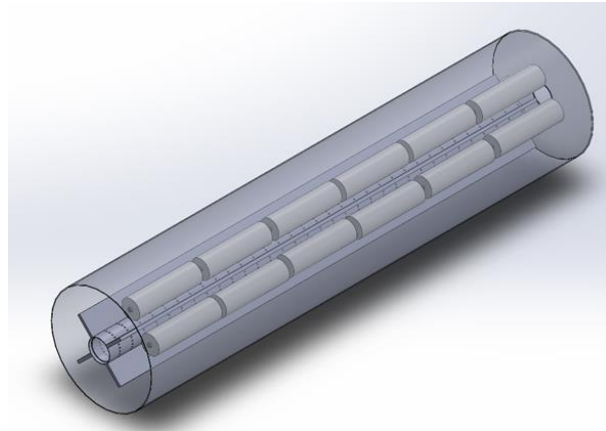
Figure 3.11 CAD model of the CWG circuit with high voltage capacitors

3.3.2.3. Tesla Coil Capacitors

Tesla coil capacitors are another type of capacitors considered for our CWG circuit Figure 3.9 (c). These capacitors are rated at 50 kV and have 50 nF of capacitance. In order to generate 80 joules, we need 8 capacitors (2 capacitors connected in parallel each at C1, C2, C3, and C4 in Figure 3. **8**(c)) . We conducted pulsed plasma discharge tests with these capacitors at 40 kV and they were robust as shown in Figure 3.12. Despite their robust performance we do not plan to use these capacitors due to their size and incompatibility in a 3-1/2" API pipe. Figure 3.13 shows the CAD model of the capacitors in the CWG circuit for larger pipe sizes (and larger drill bits) $\geq$ 3-1/2" API pipe.
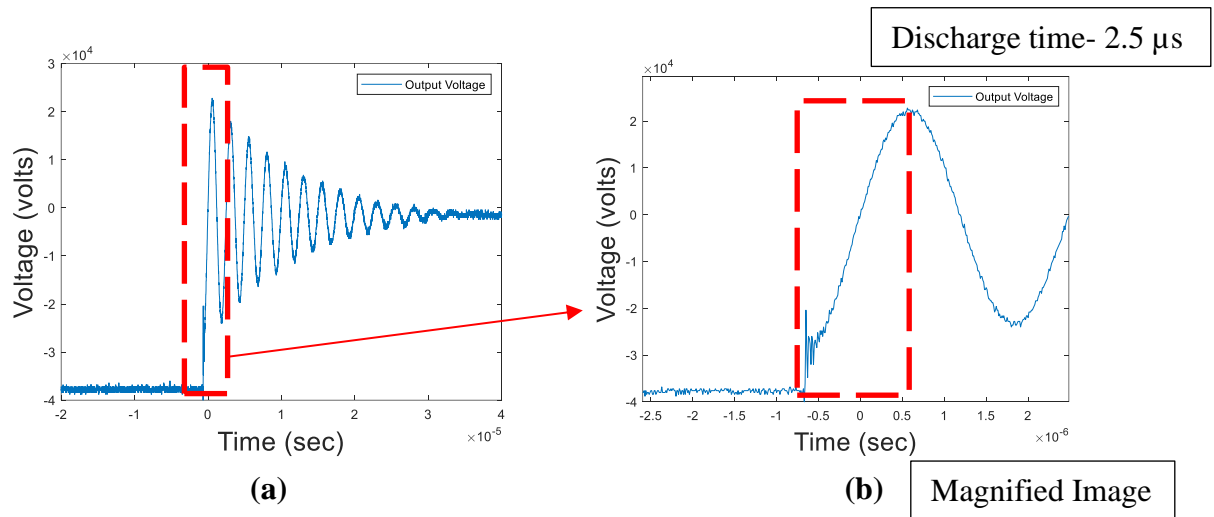
Figure 3.12 (a) Discharge test with tesla coil capacitors, Max voltage- 40400 V, Distance between electrodes - 21.25mm, Charging time- 2 to 3 sec and (b) is the magnified image of (a) showing the discharge time
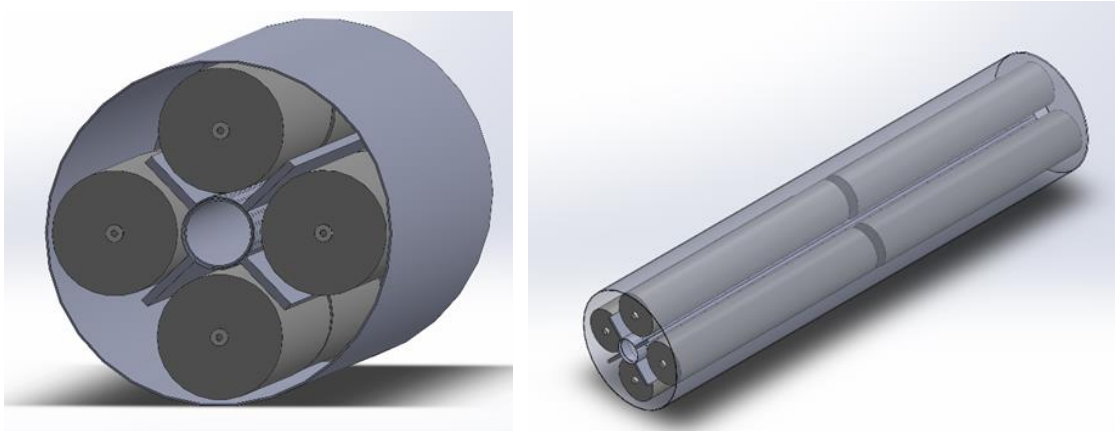
Figure 3.13 CAD model of the CWG circuit with tesla coil capacitors

3.3.2.4. Ceramic Doorknob Capacitors

The final type of capacitors which we tested in our CWG circuit are ceramic doorknob capacitors Figure 3.9 (d). These capacitors are rated at 40 kV and have 15 nF of capacitance. In order to generate 80 J, we require 28 capacitors (7 capacitors connected in

parallel each at C1, C2, C3, and C4 in Figure 3. **8**(c)). We performed pulsed plasma

discharge tests with these capacitors up to 25 kV and kept on failing above 25 kV with the

existing circuit components. After modifying the circuit with more robust diodes which

we will discuss later in the thesis we were able to test the circuit up to 35 kV. These types

of capacitors were used in our final CWG design discussed in this thesis.

3.3.3. Frictional Loss Calculations

The two main factors which we need to consider for the CWG circuit BHA form

factor design are frictional losses in the pipe due to drilling mud flow and the cavitation

number. The dimensions for inner and outer drill pipe is shown in Figure 3.14. High

frictional losses lead to high inefficiencies in the system and a lower cavitation number

leads to higher damage to the drilling pipe. In the calculations below we used a nominal

flow rate for the drilling mud of ≈100 - 500 gallons per minute (GPM), which is typical in

geothermal drilling applications [60].

Figure 3.15 shows the frictional loss calculation for different inner drill pipe

diameters at 100 and 500 GPM. The inner drill pipe diameter is chosen as one of the

variables because the frictional losses and cavitation number changes with the inner

diameter, and the maximum and minimum inner diameters are selected based on the API

dimensions of 3-1/2'' regular pin connection of the drill bit. The viscosity of the drilling

mud considered in this calculation is 18cP (centipoise), the roughness of steel pipe is taken

as 0.0018'' with a pipe length of 4ft. Different inner diameters that are considered for the

calculations are 1.5'', 1.3'', 1.1'', 0.9'', 0.7'', 0.5'', and 0.4''. The Darcy-Weisbach

equation is used to calculate the pipe frictional loss as shown in equation 3.1.

$$h_f = \frac{f\left(\frac{L}{D}\right)v^2}{2g}$$
3.1

Where, h_f is the head loss (m), f is the friction factor, L is the length of pipe work (m), d is the inner diameter of pipe work (m), v is the velocity of fluid (m/s) and g is the acceleration due to gravity (m/s²).

Outer drill pipe maximum diameter- 4-1/4"

Annulus for BHA components

Inner drill pipe
Maximum diameter- 1.5"
Minimum diameter- 0.4"

Flowing drilling mud
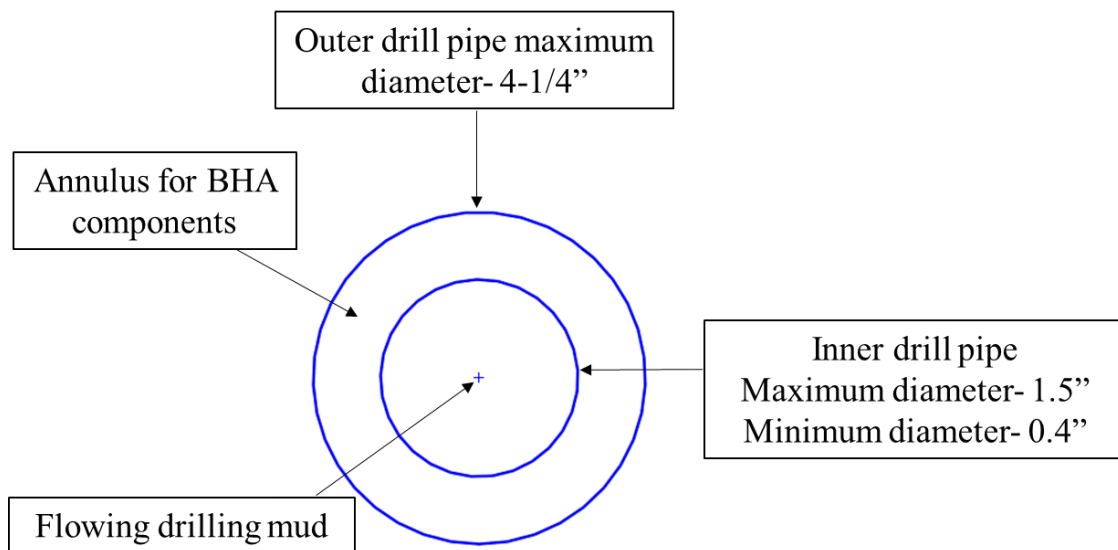
Figure 3.14 Schematic diagram for drill pipes with dimensions
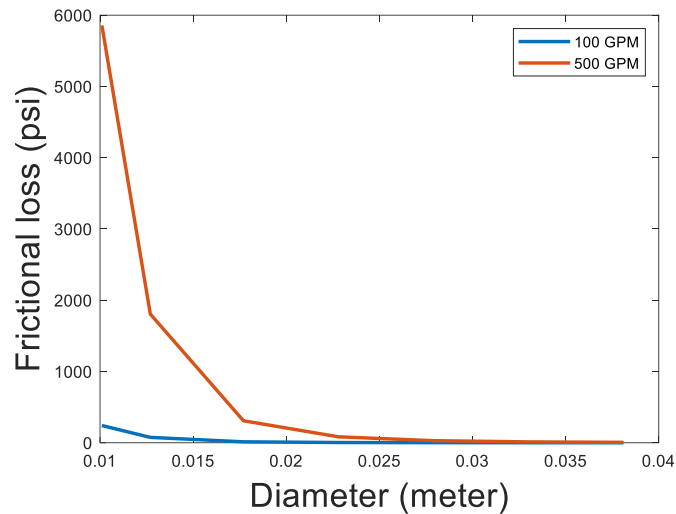
Figure 3.15 Relation between different inner diameters and frictional loss in the pipe at different flowrates

Figure 3.15 shows that as the inner drill pipe diameter decreases the frictional loss in the pipe increases which indicates that as the diameter of the pipe decreases, we have to increase the pressure of the drilling mud at the inlet (top surface) in order to get a constant pressure value of mud at the drill bit surface. Increasing the pressure results in higher pumping power requirements and higher energy consumption which is not ideal. We have to select the inner diameter as big as possible to reduce the frictional losses in the pipe.

3.3.4. Cavitation Number Calculations

The cavitation number is used to describe the behavior of voids or bubbles in a liquid. Cavitation occurs in liquids when the pressure is reduced to the vapor pressure at a given temperature of operation. Cavitation is the formation of vapor cavities in a liquid that are the consequence of forces acting upon the liquid. It usually occurs when a liquid

is subjected to rapid changes of pressure that cause the formation of cavities in the liquid where the pressure is relatively low. We calculate the cavitation number (Ca) as follows:

$$\text{Ca} = \sigma = \frac{P_\infty - P_v}{\frac{1}{2} * \rho v_\infty^2}$$

3.2

where, P_∞ is the local pressure, P_v is the vapor pressure of fluid (Pa), ρ is the fluid density (kg/m3) and v_∞ is the velocity (m/s).

The cavitation number should be high in any system as a lower cavitation number leads to significant wear of surfaces. A lower cavitation number leads to generation of bubbles or voids in the system and when the bubbles collapse, it generates a shock wave which causes repetitive cyclic stress over the metal surfaces which leads to surface fatigue.
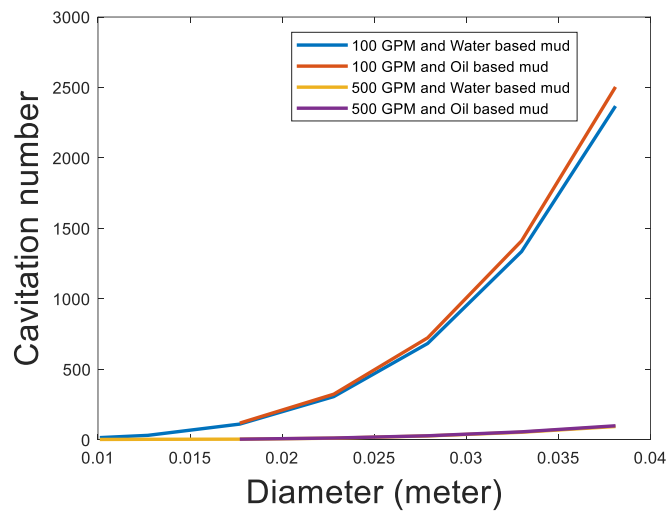
Figure 3.16 Relation between different inner diameters and cavitation number in the pipe at different flowrates and drilling mud

Figure 3.16 shows the cavitation number calculation for water-based drilling mud and oil-based drilling mud with 100 and 500 GPM flowrate for different inner diameters. The viscosity of the drilling mud considered in this calculation is 18 cP (centipoise), the roughness of steel pipe is taken as 0.0018'' with a pipe length of 48". Different inner diameters that are considered for the calculations are 1.5'', 1.3'', 1.1'', 0.9'', 0.7'', 0.5'', and 0.4''. Figure 3.16 shows as the flow rate increases (100 to 500 GPM) and diameter decreases (1.5" to 0.4") the cavitation number decreases which is not ideal for any system. In order to avoid any damage or wear to the drill pipes due to cyclic stress, the cavitation number should always be greater than 0.5 [61].

3.4. Chapter Summary

A bottom hole assembly is designed and investigated to convert hydraulic energy to electrical energy for SPARC application. Different off the shelf components (except CWG circuit) are assembled to generate pulse plasma discharges to generate microcracks over the rock surface. Different CWG circuits within the down hole form-factor are designed and tested with various capacitors and diodes to find the optimum configuration to generate 40 kV at 100 nF capacitance (80 J).

4. DESIGN AND TESTING OF CWG CIRCUIT

4.1. Energy Conversion Setup (Hydraulic to Electrical Energy)

To test the hydraulic to electrical energy conversion components of the SPARC concept, we have designed an energy conversion flow test setup. The test setup is shown schematically (Figure 4.1 (a)) and as assembled (Figure 4.1 (b)) below. The test setup consists of two parts, (a) a flow loop (Figure 4.1 (c)) and (b) an electric energy storage and step-up conversion circuit (Figure 4.1 (d)). The flow loop is intended to simulate flowing drilling fluid/mud that will be used in a typical geothermal drilling application to produce power downhole via an alternator or mud motor, and the electric circuit will be used to store the electric energy generated by the mud motor/alternator and to step-up the voltage to the required high voltage and high energy level. The flow loop consists of a multistage centrifugal pump (BVMI15-8, Berkeley Pumps) required to generate the high flowrate (≈40-60 GPM) and high inlet pressure (≈150-170 psig) required by the water turbine (PLT, PowerSpout). The turbine is a Pelton-type turbine capable of generating 1500 W at the above-stated flowrate and pressure conditions and generates a nominal voltage of ≈48 V direct current (dc) at this output power level. The flow loop is instrumented with various valves (ball valves and a globe valve) for flow control, pressure gauges, a flow meter, a pressure relief valve, and a storage tank. We tested the energy conversion setup with both water and a water based drilling mud as the working fluid. All piping in the setup is 304 stainless steel and the pump is of 304 stainless steel construction.

The output of the turbine is input into the electric energy storage and step-up conversion circuit (assembled, Figure 4.1 (d), and schematic, Figure 4.2). The electric energy storage and step-up conversion circuit components include a charge controller (FLEXmax FM60, Outback Power), battery bank (4× 12 V, 100 Ah), inverter (2 kW, AIMS Power Corp.), step-up transformer (15060P5G2, France Lighting Solutions), and a CWG. The charge controller protects the battery bank from any surges in power generation and the battery bank itself is intended (in the final application) to reduce any undesirable transients (e.g., loss of power) in the pulsed plasma generation. The inverter converts the dc voltage from the battery to 120 V ac which is stepped-up in the transformer to 10 kV ac. Finally, the positive CWG circuit converts the high voltage ac power to 40 kV dc required to generate the nanosecond plasma discharges.
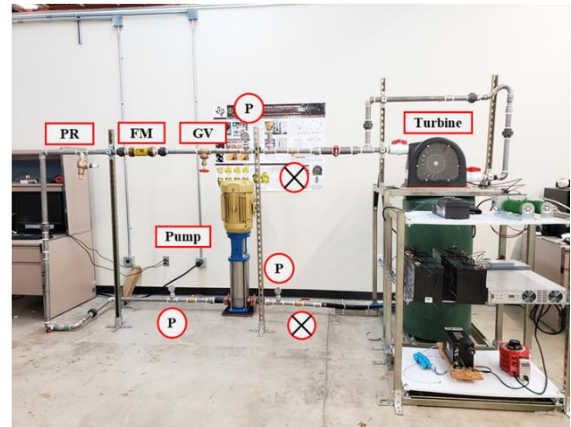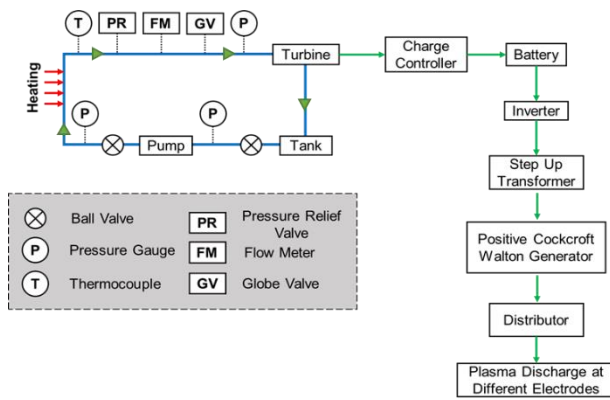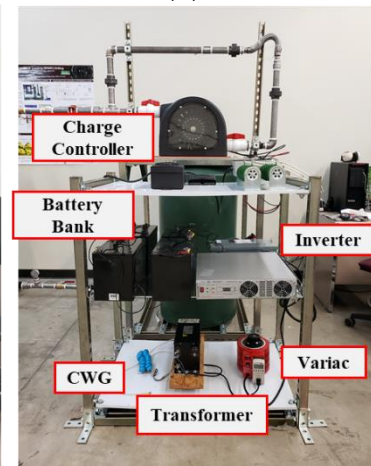
Figure 4.1 Experimental test setup for flow-to-electrical energy conversion for downhole in-situ plasma generation: (a) schematic of the test setup, and (b) image of the assembled test setup. The annotated images in (c) and (d) show the flow circuit and the electric energy storage and step-up conversion circuit, respectively.

Table 4.1 shows the efficiency calculation for various components of the energy conversion setup. The first level of energy conversion is from the pump to the turbine with an input and output power of,

$$P_{turbine\_in} = Q * h * \rho * g * \eta_{pump} \qquad\qquad 4.1$$

where, $P_{turbine\_in}$ is the turbine input power, Q is the flowrate ($9.085 \frac{m^3}{h}$), h is the differential head (70.38m), ρ is the density of fluid ($1000 \frac{kg}{m^3}$), g is the gravity (9.8m/s²) and η_{pump} is the pump efficiency (0.6).

$$P_{turbine\_out} = V * I \qquad\qquad 4.2$$

Where, V is voltage (57 V) and I is current (16.1 A)

$$\eta_1 = \frac{P_{turbine\_out}}{P_{turbine\_in}} = 52.7\% \qquad\qquad 4.3$$

The second level of energy conversion is from the turbine to the charge controller with an input and output power of,

$$P_{cc\_out} = V_{cc} * I_{cc} \qquad\qquad 4.4$$

Where V_{cc} is charge controller volatge (50.4 V) and I_{cc} is charge controller current (18.1 A)

$$\eta_2 = \frac{P_{cc\_out}}{P_{cc\_in}} = 99.4\% \qquad\qquad 4.5$$

Efficiencies for the rest of the components (batteries, inverter, and transformer) are taken from the datasheet provided by the vendor [55, 56, 57].

Table 4.1 shows that the most inefficient conversion is the pump to turbine and battery input to output. If we want to improve the overall energy conversion efficiency, we have to use a highly efficiency turbine (or alternator) along with higher efficiency batteries to convert hydraulic energy to electrical energy in an efficient manner.

Table 4.1 Efficiency calculation for energy conversion setup

	Energy Conversion	Efficiency (%)
1	Pump to Turbine	52.7
2	Charge Controller Output	99.4
3	Battery Output	85
4	Inverter Output	95
5	Transformer Output	99
6	CWG Output	90
	Total Efficiency	**37.7**
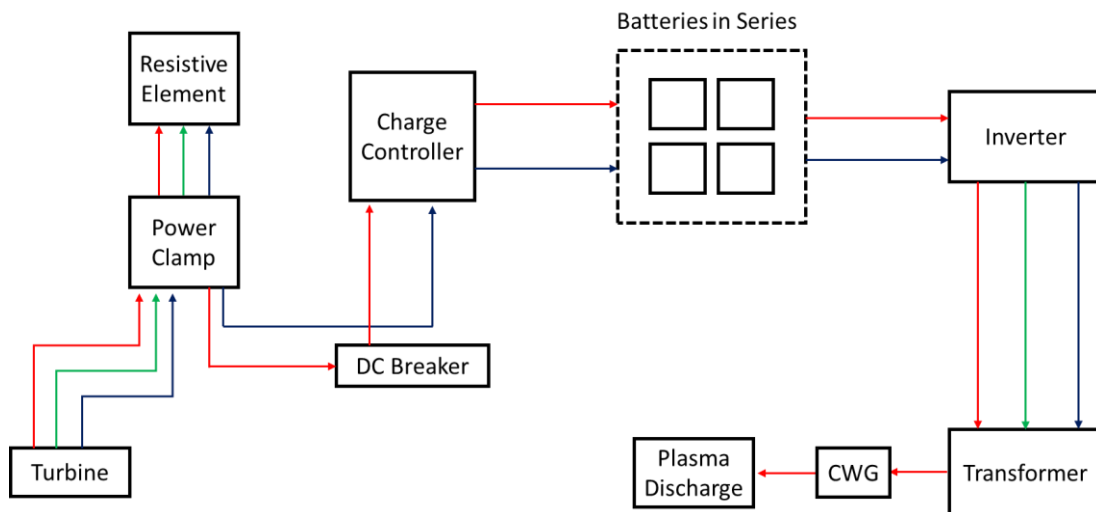
Figure 4.2 Schematic of the electric energy storage and step-up conversion circuit

4.2. CWG Testing at the Ambient Conditions

We tested a number of different CWG circuits, however, here we focus on a CWG circuit which is a two-stage circuit with a positive polarity high voltage output (Figure 4.4). Each stage consists of 10 capacitors (5 capacitors connected in parallel each at C1, C2, C3, and C4 in Figure 3. **8**(c)) and four diodes for ac-to-dc step-up and rectification. Each capacitor is rated for 40 kV and 15 nF of capacitance and each diode is rated for 40 kV and 30 mA. An image of our positive polarity high voltage output CWG circuit is shown in Figure 4. 3.
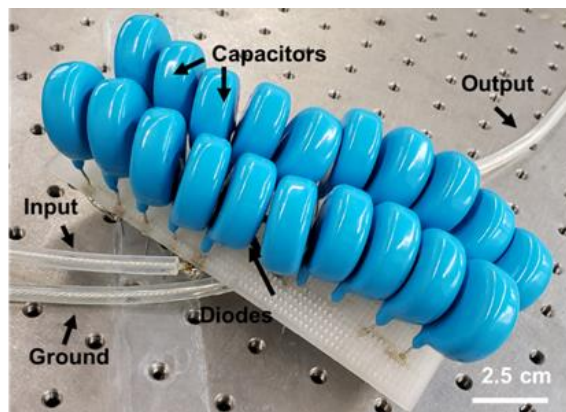
Figure 4. 3 Image of the fabricated two stage CWG circuit
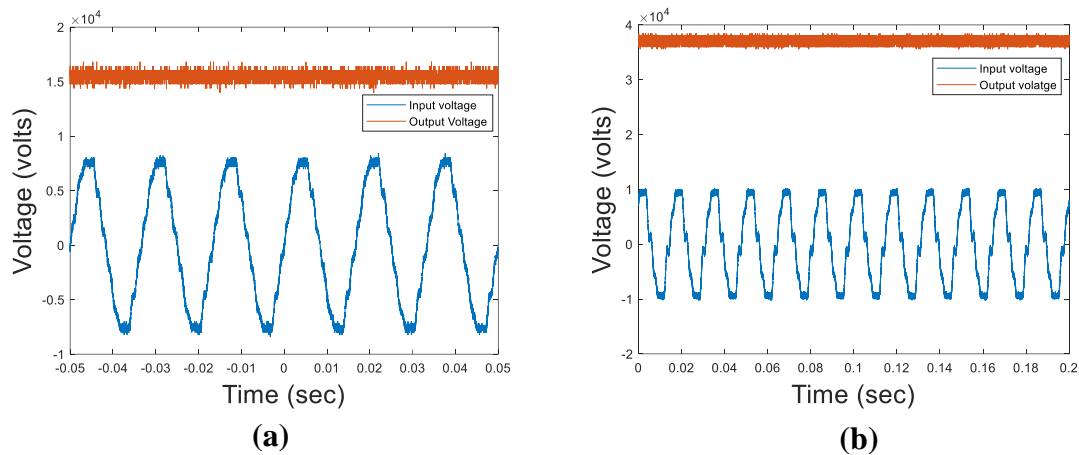
Figure 4.4 Voltage traces of the (a) single-stage positive, (b) two-stage positive output CWG circuits under no-load conditions (*i.e.*, no plasma discharge)

We tested the output of the CWG circuits operating with a plasma load (a spark discharge). An image of the characterization setup is in Figure 4.6 (a). The output of the CWG was connected to a pin-to-plate electrode setup with a voltage probe used to measure the output voltage from the CWG circuit. For these tests, the high voltage transformer was driven by the building's mains power supply through a variable ac (variac) transformer. The output of the CWG was connected to the pin electrode and the plate electrode was connected to ground. The initial charging time of the CWG circuit was found to be 140 ms when no plasma load was applied, and the capacitors are fully discharged (Figure 4.6 (b)). To initiate a plasma discharge, the plate electrode was moved toward the pin electrode, and the voltage input and the output for the CWG are plotted in Figure 4.6 (c). A magnified view of the voltage pulses during a plasma discharge is plotted in Figure 4.6 (d), and measurements indicate a repetition rate of 25 Hz with this CWG

circuit. We tested the circuit up to 15 kV as the diodes and capacitors kept on failing above this voltage. The reasons for failure are shown and discussed later in transient circuit simulations.

(a)

(b)

(c)
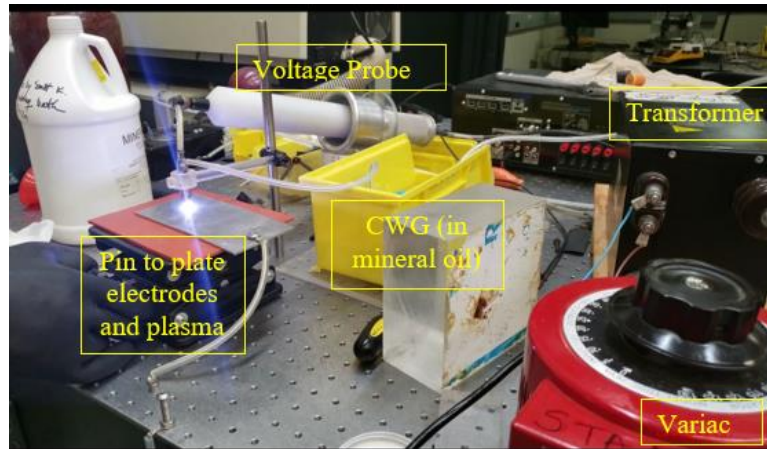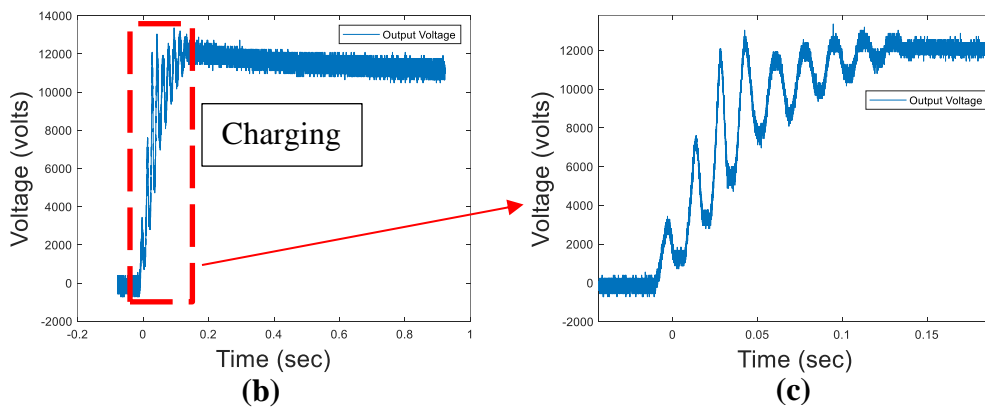
Figure 4.5 Preliminary testing of the CWG circuit: (a) image of test setup to characterize the transient capabilities of the CWG circuit under load (plasma discharge between pin-to-plate electrode configuration) conditions, (b) output of the CWG circuit under no-load conditions showing the initial charging time of the circuit to be ≈140 ms, (c) magnified view (figure b) of the charging time, (d) output of the CWG circuit under plasma load conditions, and (e) magnified view (figure c) of the

voltage traces at the output of the CWG circuit showing repetitive pulses capable of ≈25 Hz operation.

(d)   **(e)**
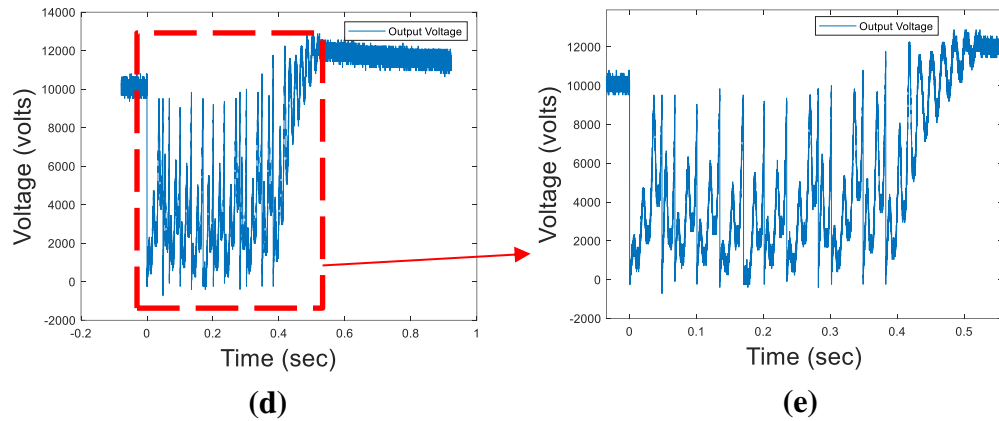
Figure 4.6 Continued.

4.2.1. CWG Testing with Durable and BHA Form Factor Components

We tested the ceramic doorknob capacitors (rated for 40 kV with 15 nF of capacitance, and high surge current) along with special high voltage diodes (rated for 60 kV and 1 A). The CWG setup contains 14 doorknob capacitors in each stage (7 capacitors connected in parallel each at C1, C2, C3, and C4 in Figure 3. **8**(c)) and 4 diodes in between as shown in Figure 4.8 (a). The test setup (Figure 4.8 (b)) contains a variac that supplies low voltage ac to the transformer which steps it up to high voltage ac and acts as an input to the CWG circuit. The CWG circuit is placed inside a plastic tub and immersed in mineral oil to insulate the diodes and capacitors. This is only a precaution since these capacitors can be operated in air. The output of the CWG is connected to the air spark gap whose length is adjustable to achieve the desired energy at the SPARC electrodes. The air

48

spark gap simulates the distributor in the actual SPARC application. Figure 4.8 (c) shows

the circuit diagram of CWG testing setup at ambient conditions.

(a)

(b)
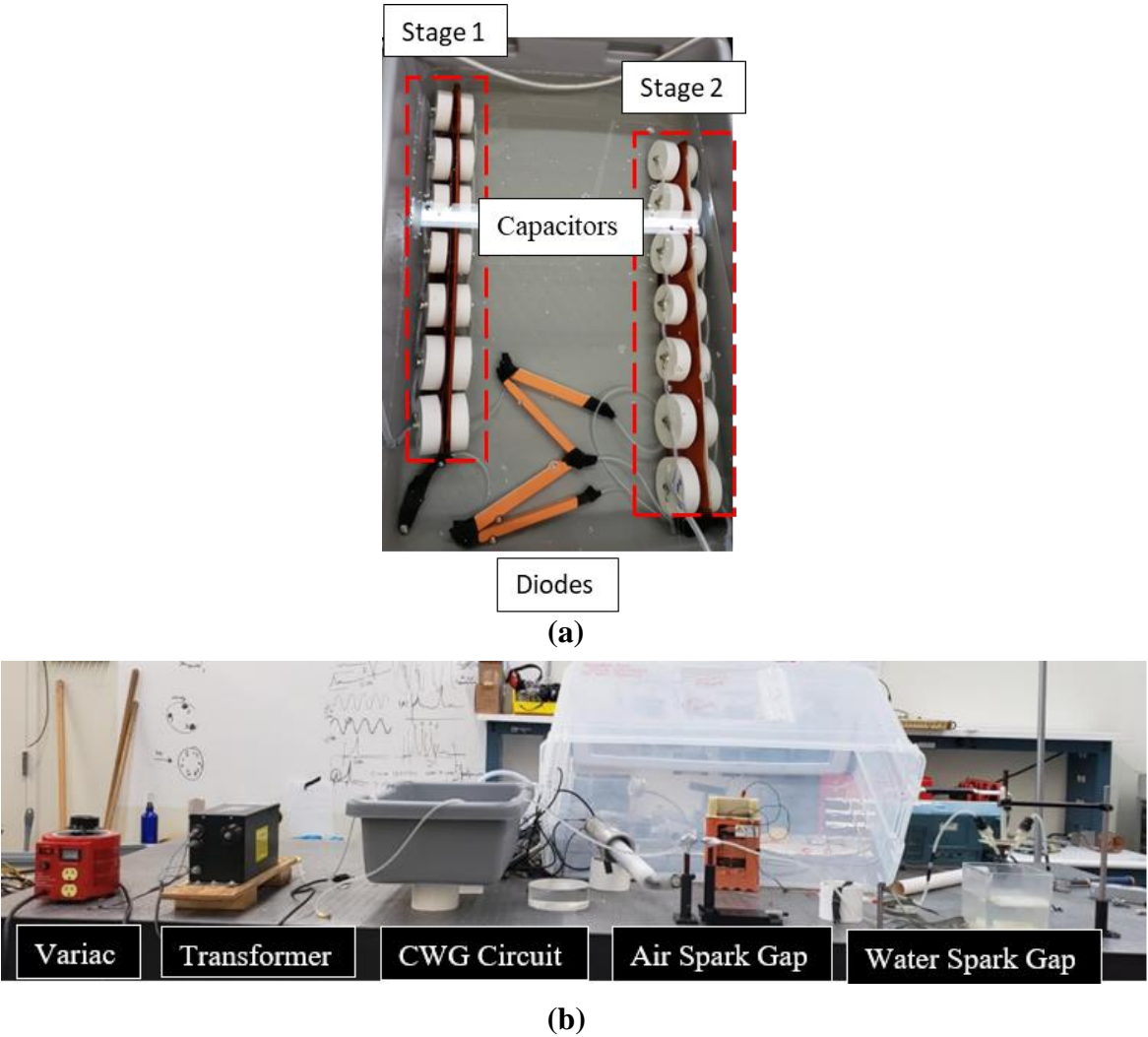
Figure 4.7 (a) Two-stage CWG circuit with doorknob capacitors and diodes inside mineral oil, (b) test setup for room temperature CWG testing, (c) circuit diagram of the test setup
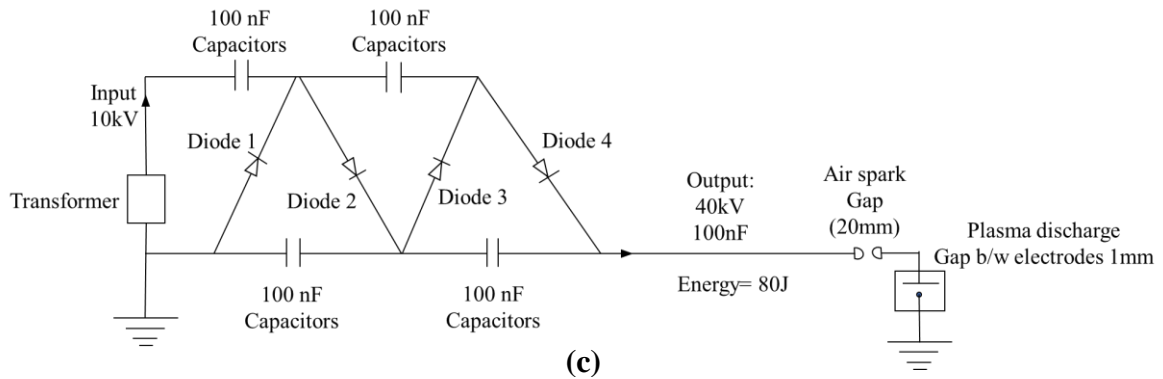
Figure 4.8 Continued.

We characterized the CWG circuit at ambient conditions of 1 atmosphere and room temperature of 70 °F, and the results are shown in Figure 4.10 (a). For the first test, the variac was kept at 48 V which was connected to the transformer. The transformer stepped up it to ≈3750 V which was then input to the CWG. The distance between the two electrodes pairs (stainless steel for the air spark gap, and tungsten for the SPARC water discharge) set at 4.3 mm and 1 mm respectively. The distance between the electrodes fixes the discharge voltage and is dependent on the medium in which we are generating plasma (dielectric strength changes with the medium). Larger the distance between electrodes, higher the voltage needed to ionize the medium (air and water) or to generate plasma. The first discharge was performed at 15 kV. In the subsequent tests, the distance between the electrodes were kept constant but the input voltage to the CWG circuit was increased. As the voltages increased at the same air electrode spark gap, the time needed to ionize the air decreased. Because of this, the charging time decreased and the frequency of the discharges increased from 1 Hz to 5 Hz which is shown in Figure 4.10 ((a), (c) and (e)). For the second test, the variac was kept at 66 V, and the transformer output was 5500 V

which was the CWG input. In this test the air electrode gap was increased to 6.5 mm and water electrode gap was kept constant at 1 mm. The pulsed plasma discharges had peak voltages of 22 kV, however the frequency decreased as shown in Figure 4.10 (g).
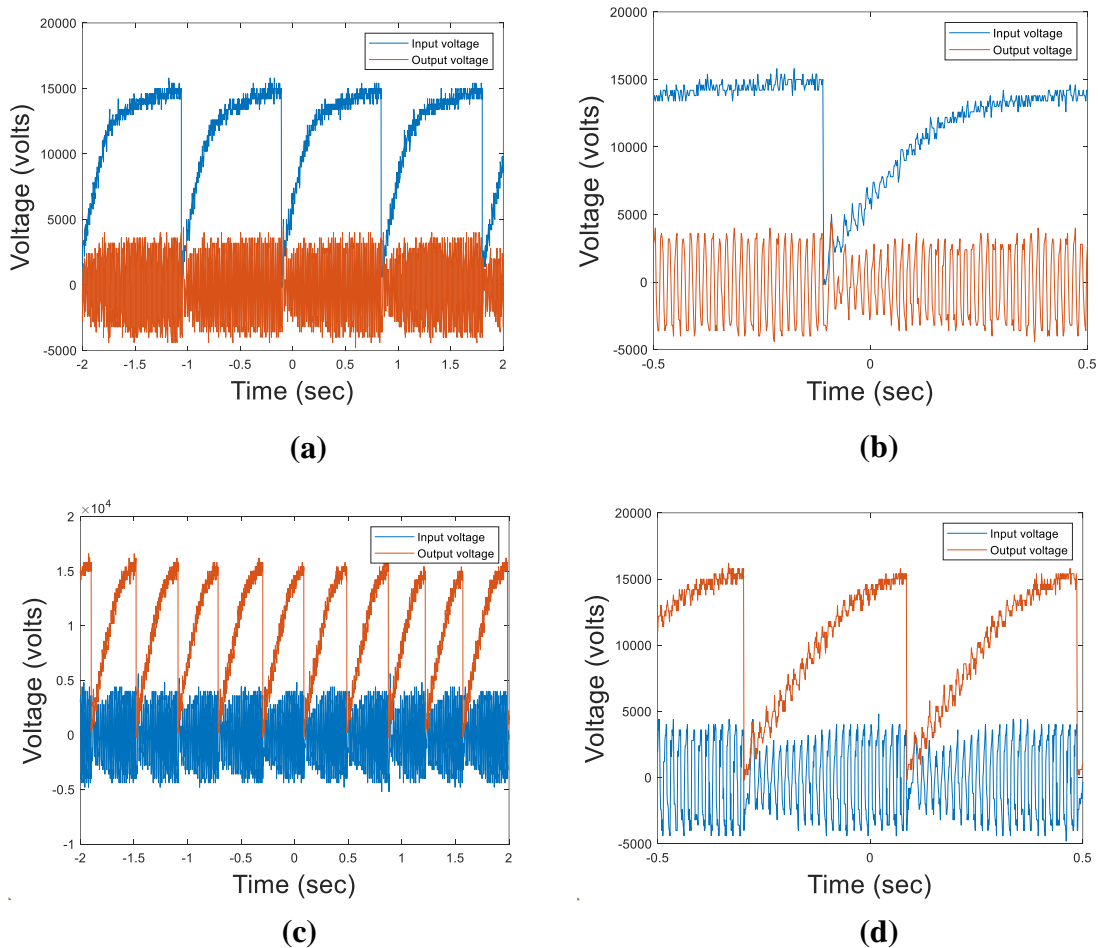
Figure 4.9 (a) Time vs Voltage graph for a discharge voltage of 15 kV and discharge frequency of 1 Hz (b), (c) Time vs Voltage graph for a discharge voltage of 15 kV and discharge frequency of 3 Hz (d), (e) Time vs Voltage graph for a discharge voltage of 15 kV and discharge frequency of 5 Hz (f), (g) Time vs Voltage graph for a discharge voltage of 22 kV and discharge frequency of 1 Hz (h)
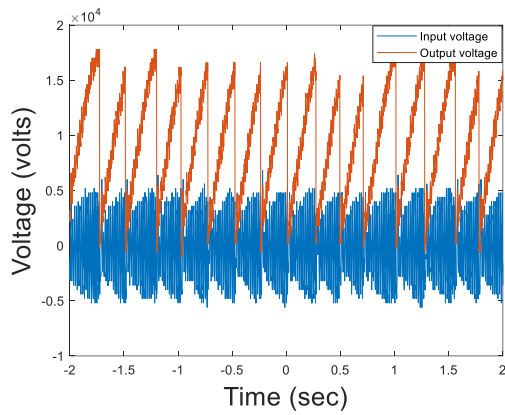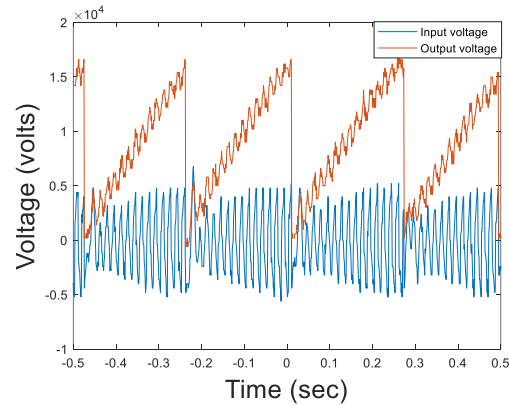
(e)   (f)
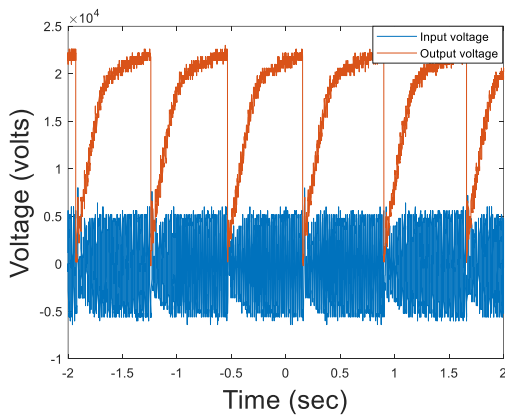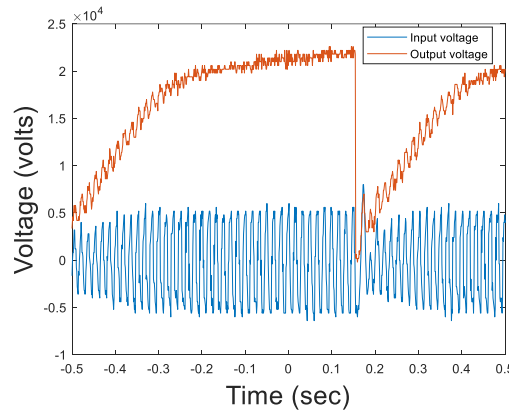
(g)   (h)

Figure 4.**10 Continued.**

4.3. Circuit Simulation of CWG Setup

To guide our CWG design for further downhole conditions we also simulated the CWG circuit using a circuit simulator program (LTSpice) [62]. LTSpice is a circuit simulator from Analog devices which allows one to draft, probe, and analyze the performance of any circuit design. Simulations of different iterations of the CWG circuit allows us to explore circuit limitations and performance boundaries of the design through

minor adjustments. The other benefit of using LTSpice is to enable predictions for our CWG circuit output at conditions that may not be possible to test experimentally.

4.3.1. LTSpice Simulation of CWG Setup

We simulated a CWG circuit that has all the electrical components as the actual experiments and the LTSpice block diagram is shown in Figure 4.11. The LTSpice model has five major components. (i) An ac source at 10 kV peak voltage and 60 Hz. In the LTSpice model the ac source replaces the variac and transformer used in the experiments. (ii) A CWG voltage multiplier circuit. The CWG converts the 10 kV ac to 40 kV dc with a pulsing energy of 80J. This circuit contains four capacitor banks rated at 40 kV of 105nF capacitance and four diodes. (iii) An air spark gap which simulates two electrodes at a specified distance (≈20 mm in air) in actual experiments. In the LTSpice model, the air spark gap is represented by a voltage-controlled switch which completes the circuit (ionizes the air) once the output voltage from the CWG reaches 40 kV. (iv) A liquid spark gap which simulates two electrodes (positive and ground) at some distance in liquid which in this case is water. In the LTSpice model it is represented by a voltage-controlled switch which completes the circuit (generates plasma in liquid) once the voltage reaches 39 kV. (v) A voltage probe and oscilloscope, where the probe is used to measure the input and output voltage of the CWG and the oscilloscope displayed the corresponding signals as waveforms. In order to ensure that the simulations were representative of experiments, we also included the inductance value of high voltage wires used and the resistance and capacitance of the high voltage probe used in the tests.
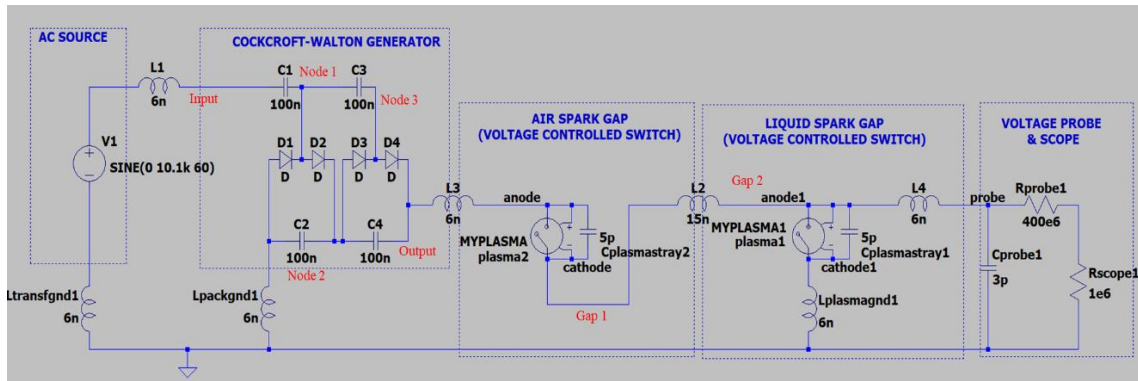
Figure 4.11 Circuit diagram for two-stage CWG setup with air and water spark gap

Figure 4.13 (a) shows the simulation predictions at each stage of the CWG including the output voltage for an input voltage of 10 kV. Figure 4.13 (b) shows the energy dissipation at the air spark gap with respect to time and the plasma pulse has an energy of ≈80 J. Figure 4.13 (c) and Figure 4.13 (d) show the variations in voltage at the output, after the air spark gap and after the liquid spark gap with respect to time. We can post-process the data in order to estimate the charging time as well as discharging time from these waveforms. The charging time is the time taken by the capacitors in order to get fully charged at 40 kV (discharge voltage) and it is 0.45 sec for our circuit and the stated operating conditions. The discharge time is the time taken by the capacitors to get discharged from 40 kV to 0 V which is 18 μs for our load. Figure 4.13 (e) shows voltage vs time and current vs time at the liquid spark gap and Figure 4.13 (f) is a magnified view to highlight the variations at shorter timescales. From this plot, we can also see that the maximum current at the second spark gap is around 1700 A.

54

We validated the model with experimental measurements and single stage CWG. Figure 4.13 (g) shows experimental measurements for the input voltage, and the output voltage and current for the CWG which is compared with the simulation predicted values of the current and voltage at air spark gap. As the experiment was done on a single-stage CWG with an input of 6.5 kV, the output was ≈13 kV with a peak current of ≈900 A which is 11.1% higher than the simulation value of current (≈800 A) as shown in Figure 4.13 (h). This means specification (voltage/current rating) of each component of the CWG should be selected by taking a tolerance of ±11%.

(a)   (b)
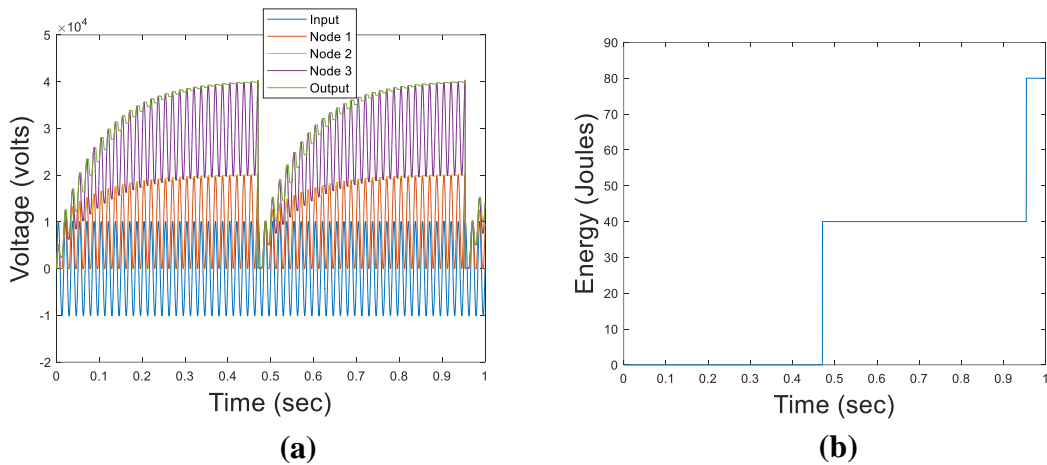
Figure 4.12 (a) shows the simulation predictions at each stage of the CWG, (b) shows the energy dissipation at the air spark gap with respect to time, (c) and (d) shows the variations in voltage at the output, after the air spark gap and after the liquid spark gap with respect to time. (e) shows the relation between the voltage and current at the liquid spark gap. (f) is a magnified view to highlight the variations at shorter timescales. (g) shows experimental measurements for the input voltage, and the output voltage and current for the CWG, (h) shows the relation between the voltage and current at the air spark gap
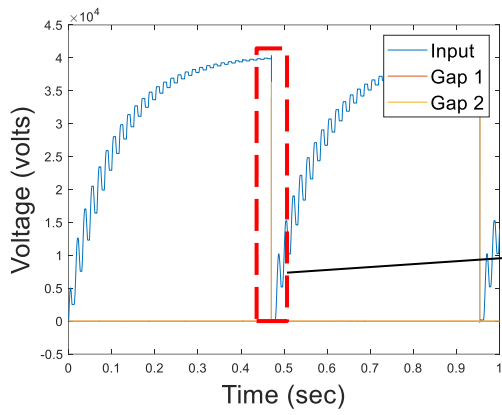
(c)
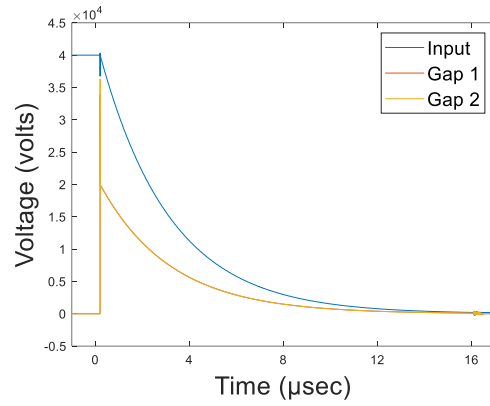
(d)
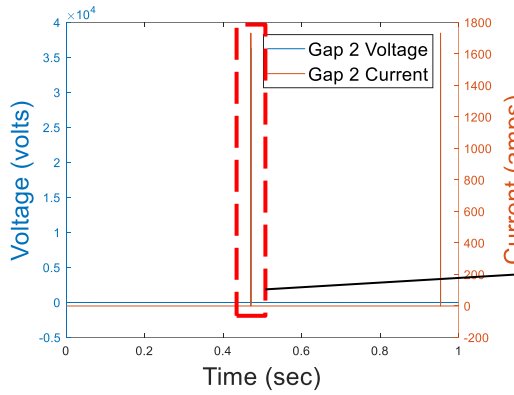
(e)
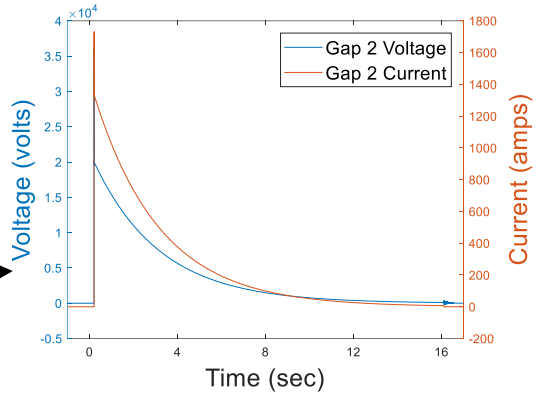
(f)
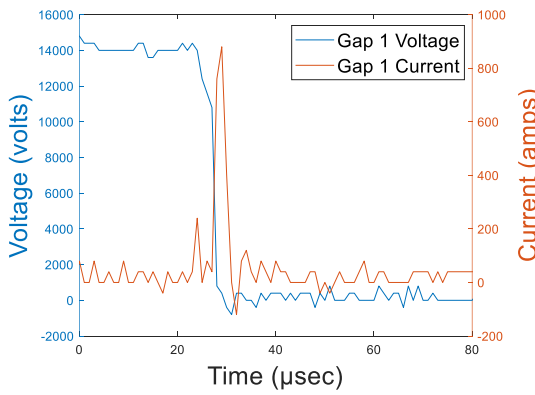
(g)
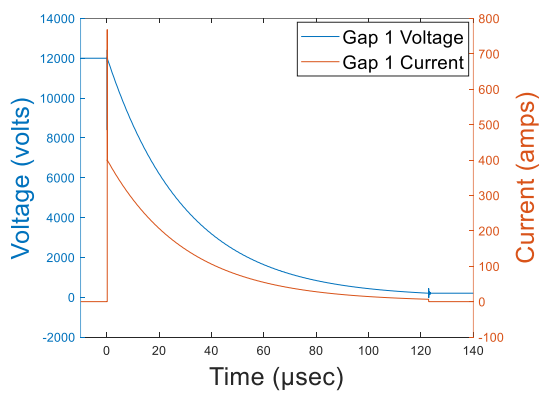
(h)

Figure 4.13 Continued.

The circuit simulator was also helpful in diagnosing unexpected experimental outcome. We tested the new doorknob capacitors along with special high voltage diodes. Each of the diode is rated for 60 kV and a maximum current of 1 amp as shown in Table 4.2. The tests operated as expected up to voltages of 25 kV ($\approx$30 J per pulse), however beyond these voltages the circuit failed. In order to understand the reason of failure despite appropriate voltage ratings on all components, we simulated the performance of the existing circuit in the modeling tool LTSpice (circuit diagram in Figure 4.11). Figure 4.15 (a),(b),(c), and (d) shows the current experienced by different diodes with respect to time when the input voltage to the CWG is 6.25 kV and the output voltage is 25 kV and Figure 4.15 (e),(f),(g) and (h) shows the current experienced by different diodes when the input voltage to the CWG is 10 kV and the output voltage is 40 kV. From the figure, it is clear that the maximum current at diode 1,2,3 and 4 are 0.25, 140, 12.5, and 550 A respectively when the output of CWG is 25 kV and 0.5, 230, 6.5 and 880 A when the output of CWG is 40 kV. Our modeling and analysis show that the main reason for CWG failure is the surge current experienced by diodes 2, 3, and diode 4 which were not rated for these high surge currents. For such a high surge current, there are three risks, (i) such a brief current may cause a concentrated hot spot in the diode that the diode mechanically fractures/breaks due to thermal expansion of materials, (ii) the fast and high magnitude nature of the pulse may stress the diode enough to physically damage it and (iii) if there is insufficient heat sinking, the diode may go into thermal runaway conditions which will also physically damage the diode and packaging. Figure 4.15 (i) and (j) shows that the surge current experienced by each capacitor (C1, C2, C3 and C4) is 550 and 880 A when

57

the output of CWG is 25 kV and 40 kV respectively. Figure 4.15 (k) and (l) shows that

the voltage across each diode (D1, D2, D3 and D4) is 13 kV and 20 kV when the output

of CWG is 25 kV and 40 kV respectively and is important to consider in our designs. The

current experienced by each component of the CWG for this small duration is very high

and because of that all the components of the CWG should be rated for high surge current.

Table 4.2 Voltage and current ratings for the existing components

Name	Voltage (kV)	Current (A)
Ceramic Capacitor	40	-
D1	60	1
D2	60	1
D3	60	1
D4	60	1
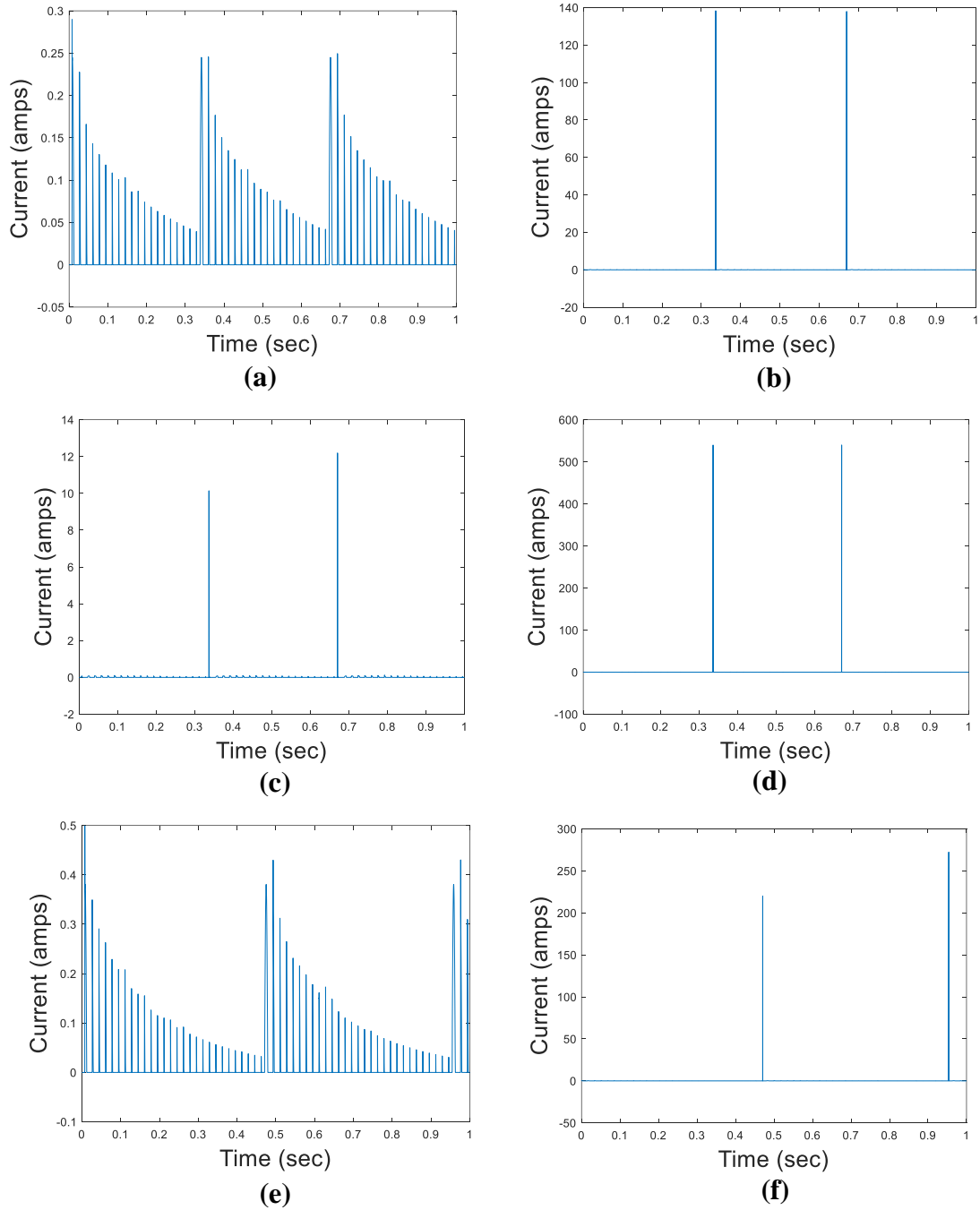
Figure 4.14 (a), (b), (c), and (d) shows the current at diode 1, 2, 3, and 4 respectively when the output voltage of CWG is 25 kV, (e), (f), (g) and (h) shows the current at diode 1, 2, 3, and 4 respectively when the output voltage of CWG is 40 kV, (i) and (j) shows the current at each capacitors when the output voltage of CWG is 25 kV and 40 kV respectively and finally (k) and (l) shows the voltage across each diode with respect to time when the output voltage of CWG is 25 kV and 40 kV respectively
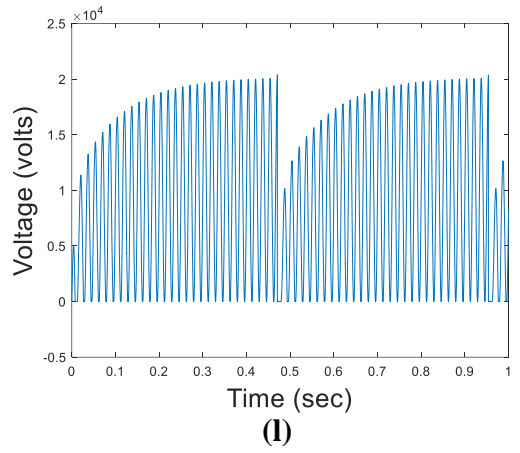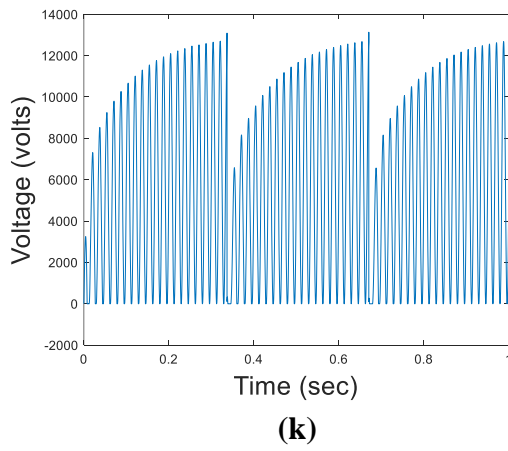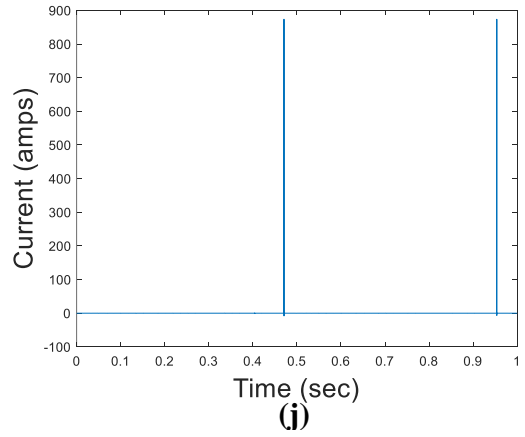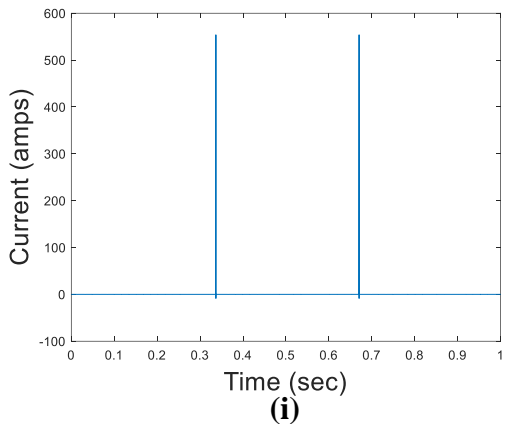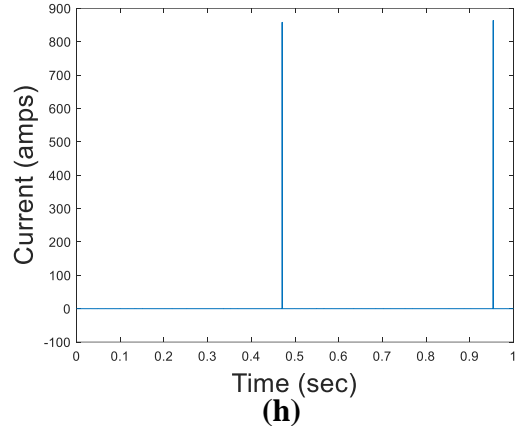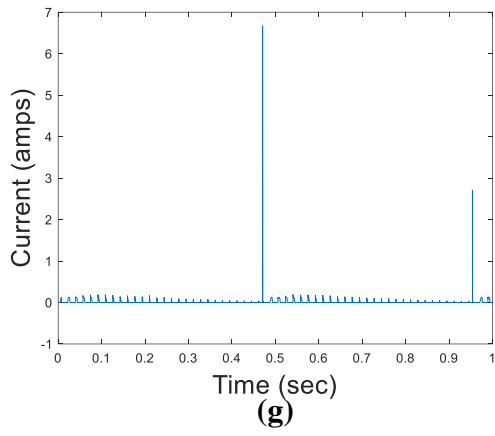
Figure 4.15 Continued.

Based on the shortcomings of the existing circuit, specifically the surge current rating on the diodes, we arrived two potential solutions. The first is to use inductors in the circuit after each diode which will resist sudden changes in the electric current flow through the circuit. Based on our calculations we would need a 15 mH inductor after each diode to reduce the current surge magnitude as shown in Figure 4.16(a). This inductor would require a 40 kV voltage rating, a BHA form factor, and high-temperature operation capabilities, however, such an inductor is currently not commercially available. Finally, the inclusion of an inductor would increase the pulse width of the plasma which is undesirable for this energy focusing application. Our second solution was to re-design the diode components of the circuit to meet the required voltage and surge current ratings specific to the conditions that a particular diode faces. For example, we will replace diode 4 with a diode assembly that consists of multiple diodes in series and parallel. This allows us to meet the rating requirements for the different diodes (Table 4.3, Figure 4.16(b)) based on the diode ratings. Additionally, even though the diode voltage ratings required are 20 kV, we are designing our setup for 40-50 kV to introduce a factor of safety. Figure 4.16(c) shows the discharge time for the new/updated circuit as modeled in LTSpice, and the model results show that this new arrangement of diode assemblies does not affect the plasma characteristics. Figure 4.16(d) shows the shows the energy dissipation at the air spark gap with respect to time, and we can see that the maximum energy dissipation is ≈80 J, as required for the SPARC application.

61
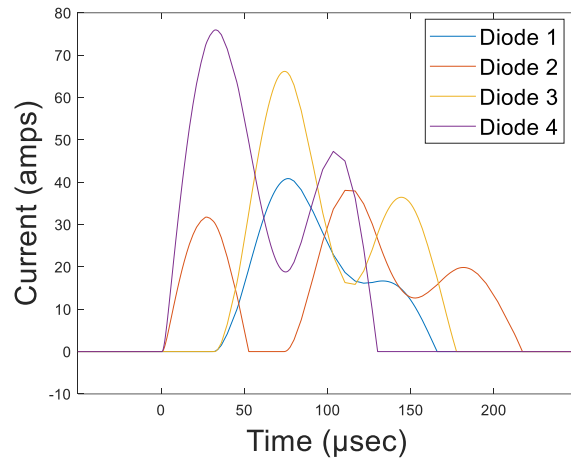
(a)
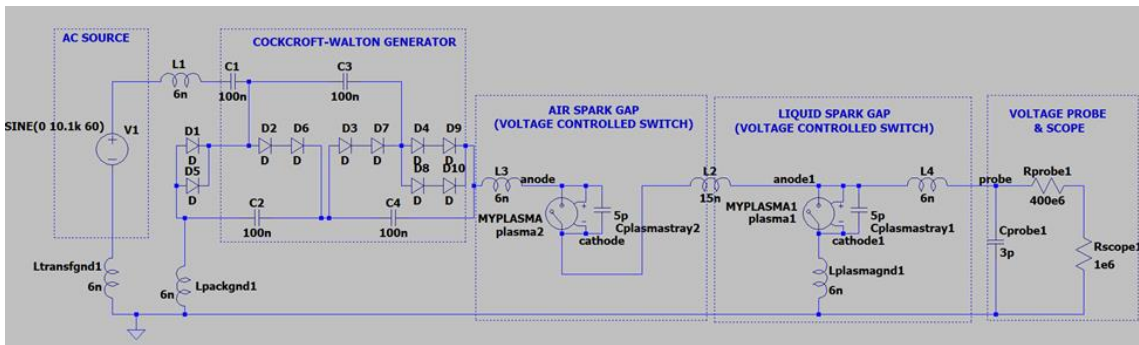
(b)
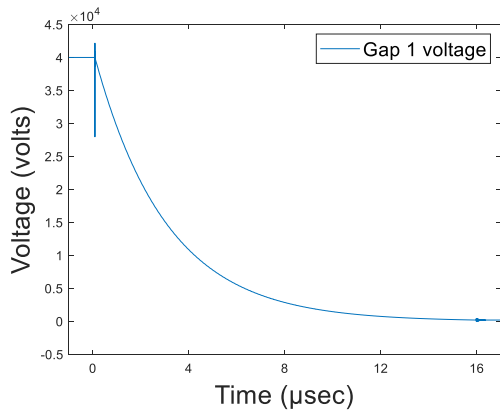
(c)
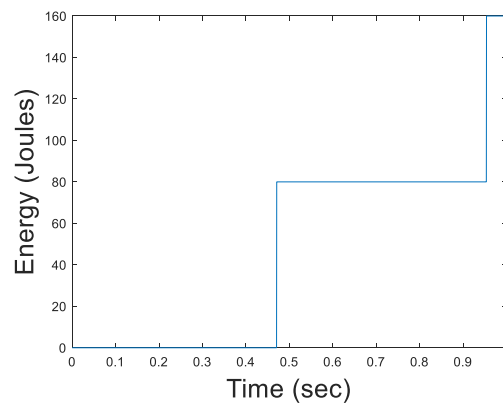
(d)

Figure 4.16 (a) shows the current at diode 1, 2, 3, and 4 with time after using inductors (b) shows the new circuit diagram with different diodes at different positions, (c) shows the relation between the discharge voltage and time at the air spark gap (d) shows the energy dissipation at the first spark gap with respect to time.

Table 4.3 Voltage and current ratings for the new circuit components

Name	Voltage (kV)	Current (A)	Series	Parallel	Total Quantity
D1	60	2	-	2	2
D2	50	800	2	-	2
D3	50	800	2	-	2
D4	50	1600	2	2	4

After rectifying the problem, we are currently testing the new CWG circuit design (diodes in series and parallel). We tested the circuit up to 35 kV without any problem and the result is shown in Figure 4.17(a,b).

(a)   (b)
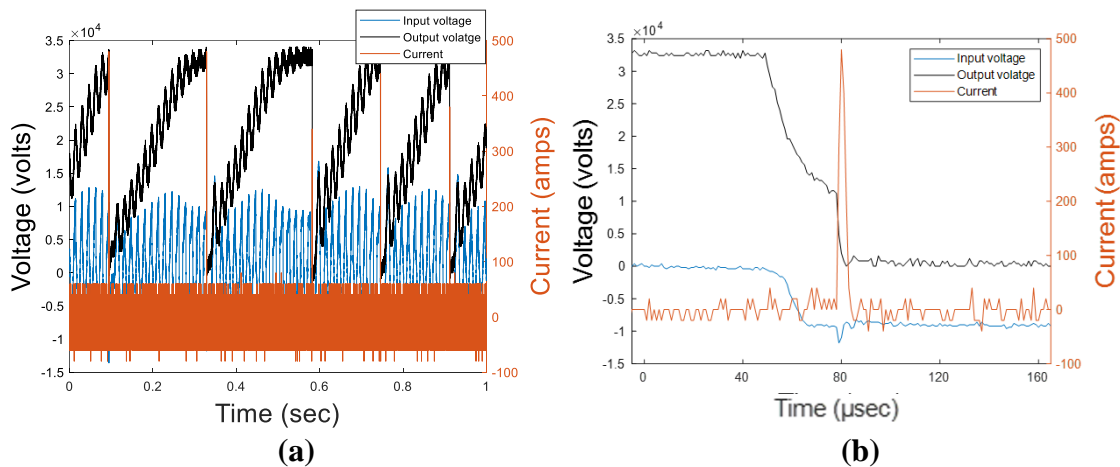
Figure 4.17 (a) New CWG circuit testing at 35 kV in ambient conditions, (b) magnified image of (a)

4.4. CWG Circuit Testing at High Temperature

In order to test the hydraulic/flow-to-electrical energy conversion setup in geothermal relevant drilling conditions, we researched different drilling fluids and we designed a test setup to characterize the CWG performance under high temperature (≈200-250 °C) operating conditions. In this section we discuss the characterization/design of the CWG circuit at high temperature, the heat loss calculation through the test setup at high temperature and selection of a dielectric fluid for these high temperature tests.

4.4.1. Design of High-Temperature CWG Testing Setup

The operation of a CWG at high temperature is currently unknown and no commercial products are available. In order to characterize its performance at high-temperature conditions (200-250ºC), we have designed a custom test setup and circuit. Figure 4.19 (a) shows the schematic diagram of the high-temperature CWG setup where a low input voltage (120 V ac) is converted to high voltage (10 kV ac) using a transformer which acts as the input to the CWG circuit. The CWG circuit (combination of diodes and capacitors Figure 3. **8**(c)) is placed inside a stainless-steel pipe (class 150) which can be temperature controlled to ≈200ºC using fiberglass heaters. Appropriate insulation is provided to reduce heat loss from the setup to the environment. The CWG generates pulsed plasma discharges of 80J per pulse (40 kV and 105 nF). Four T-type thermocouples are connected to the setup where two are placed inside the pipe and two are placed on the outer surface of the pipe to measure temperature during testing. A pressure gauge is also connected to the flange to measure pressure inside the pipe during the experiment. High voltage input, output and ground wires are connected to the setup through SS304 cord grip

feedthroughs. Increasing the temperature of the setup will lead to outgassing of the components (dielectric fluid, circuit, etc.) and in order to prevent catastrophic pressurization, a rupture disc mechanism rated for 150 psi is installed in the setup. Along with this a 1/4" NPT-to-tube compression fitting is also installed to vent the system when the pressure exceeds a threshold limit of ≈30 psig (Figure 4.19 (b)).

(a)
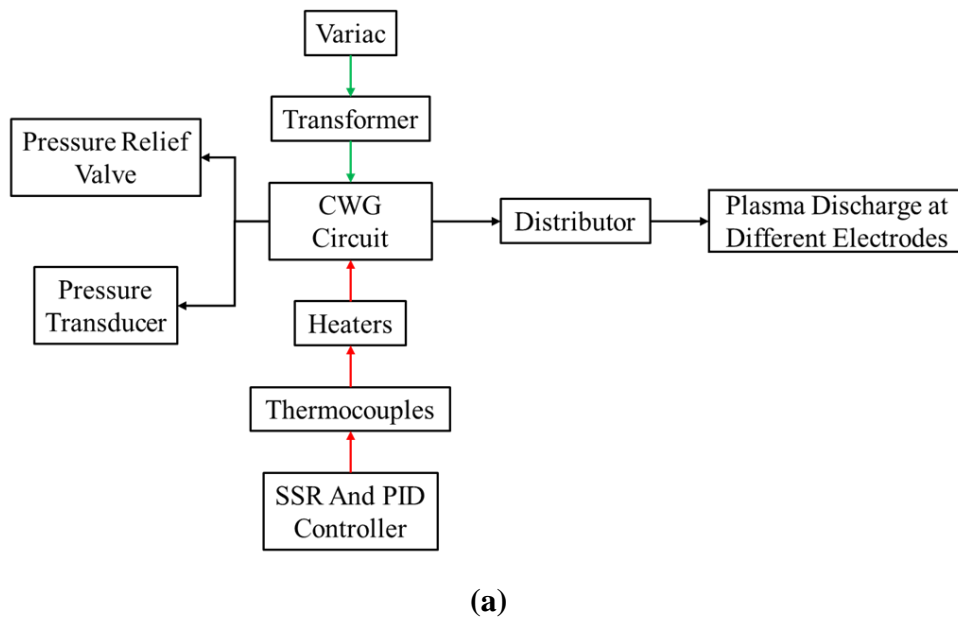
Figure 4.18 (a) Schematic diagram of the high-temperature CWG setup, (b) CAD model of the flange for high-temperature CWG testing, (c) Fabricated flange with major components

(b) **(c)**
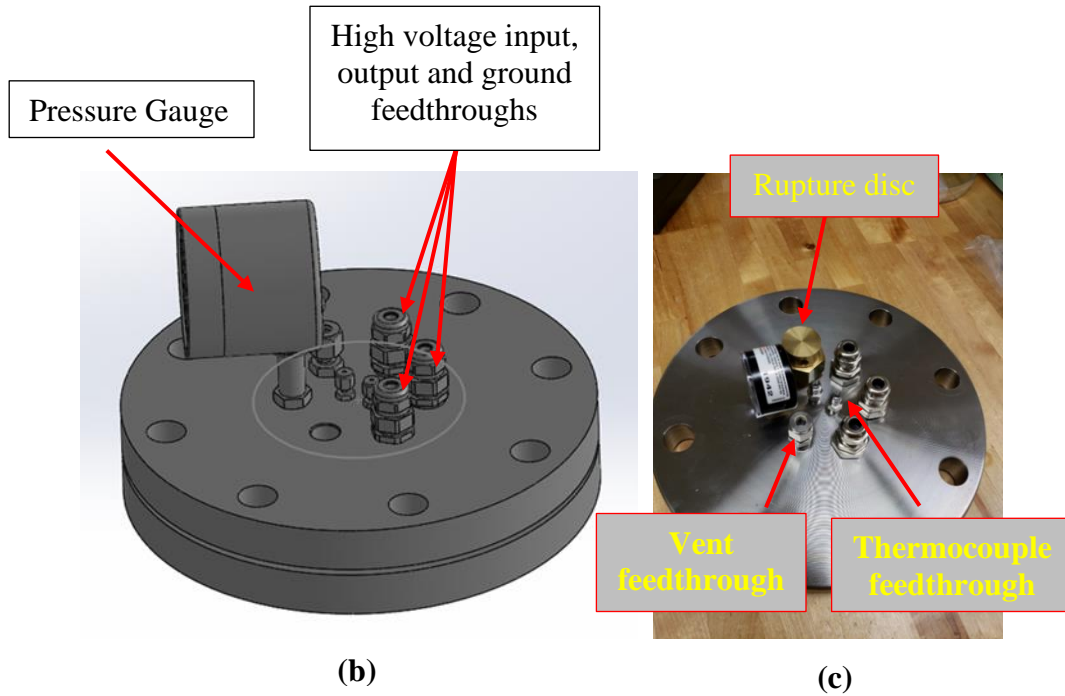
Figure 4.19 Continued.

In Figure 4.20 (a), we show the 3D model of the two-stage CWG type of BHA form factor. The capacitors used here are ceramic doorknob capacitors that have materials capable of higher temperature operation in air. The CWG is mounted onto a garolite sheet and housed in the pipe enclosure. The schematic diagram of the test setup and the configuration/form factor of the CWG is shown in Figure 4.20 (b).
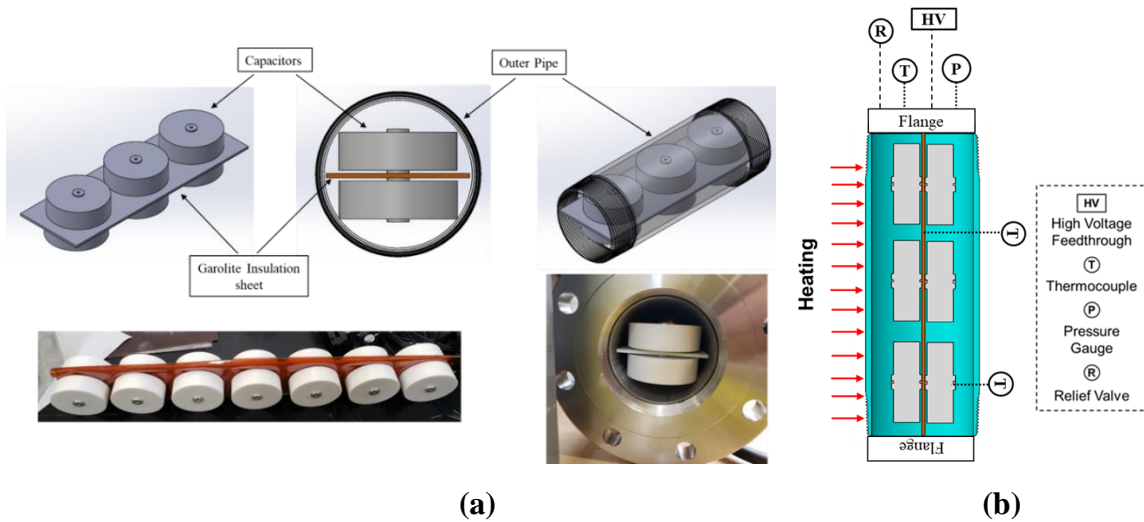
Figure 4.20 High-temperature CWG test setup: (a) 3D model of the high-temperature CWG test circuit in a downhole form factor, and (b) schematic diagram of the test setup with major components.

Figure 4.21 (a) shows the CAD model of the high-temperature CWG test setup which consists of a 48" long pipe and a 36" long pipe (both SS304), and the ends are capped with flanges. We designed this setup to be modular so as to enable additions (additional CWG circuits) to the setup in the event that high temperatures lead to a de-rating of the capacitors. The assembled system with all components is shown in Figure 4.21 (b). Six fiberglass rope/band heaters (each ≈520 W) are used to enable temperature control of the test setup which will contain mineral oil within the pipes to increase the thermal transport from the heaters to the CWGs. Figure 4.21 (c) shows the assembled view of the high-temperature CWG setup with the temperature control electrical circuit. This electrical circuit consists of two PID controllers and two solid-state relays (SSRs). To reduce the heat loss from the setup during high-temperature operation, we have insulated

the outer surface with fiberglass paper insulation, and in order to electrically insulate the

inner surface of the pipe, we will insert a Kapton polyimide film on the pipe inner wall.

(a)

(b)

(c)
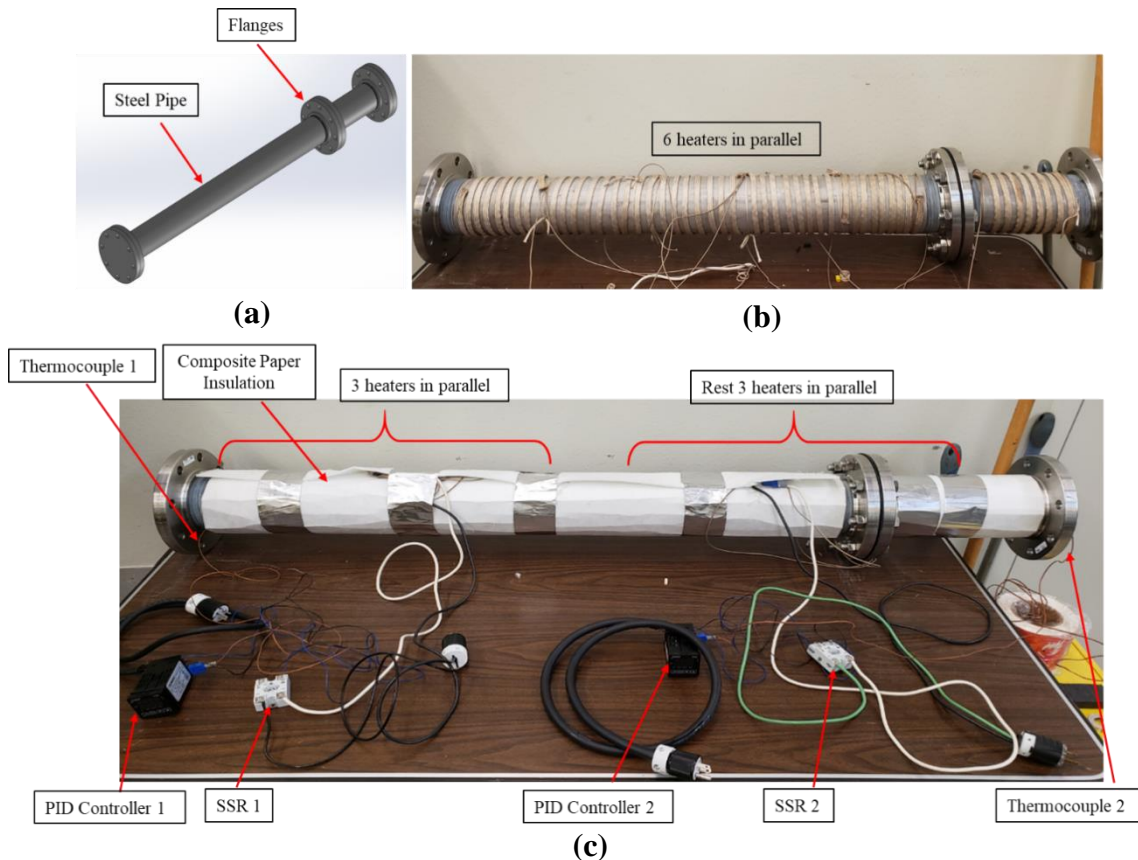
Figure 4.21 (a) CAD model of the modular high temperature CWG setup and heaters connected in parallel on the circumference of the pipes (b). (c) shows the assembled view of the high temperature CWG setup with the temperature control electrical circuit

4.4.2. Heat Loss Calculation Through the Pipe

The SPARC application downhole will see temperatures exceeding 200°C. As the

experiments are being performed at high temperature, we need to manage heat losses from

the pipe surfaces to the environment via convection and radiation. The calculation shown below specifies the total heat loss from the system with insulation and without insulation. This calculation was necessary to finalize the type of insulation being used in the setup (material, size, thickness, etc) along with the heater specifications required to achieve the required operating temperatures ($\approx$250 °C). Figure 4.22 shows the thermal resistance network for heat transfer through the high temperature CWG setup to ambient. Heat loss via convection and radiation will occur from the pipe surface to the ambient. The temperature of the heater surface temperature is ($T_{Surface}$) 250°C and temperature of the ambient ($T_{Ambient}$) is 20°C.
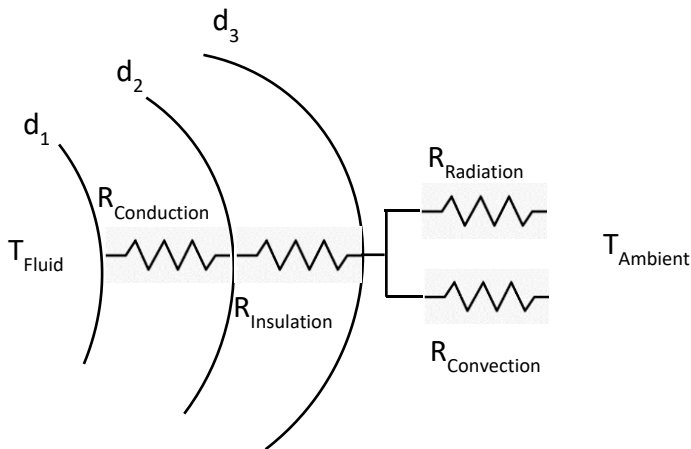
Figure 4.22 Resistance network for heat loss calculation

$$R_{Effective} = R_{Conduction} + R_{Insulation} + R_{Combined\ (Convection\ +\ Radiation)} \qquad 4.6$$

$$\frac{1}{h_{eff}A} = \frac{\ln\left(\frac{d_2}{d_1}\right)}{2\pi L K_{wall}} + \frac{\ln\left(\frac{d_3}{d_2}\right)}{2\pi L K_{insulation}} + \frac{1}{h_{combined}A}$$ 4.7

$$Q_{loss} = h_{eff} * A * (T_{Surface} - T_{Ambient})$$ 4.8

where, $R_{Effective}$ is the overall thermal resistance of the system, $R_{Conduction}$ is the thermal resistance due to conduction, $R_{Insulation}$ is the thermal resistance due to the insulation, $R_{Combined}$ is the thermal resistance due to both convection and radiation, Q_{loss} is the heat loss in the system, h_{eff} is the overall heat transfer coefficient of the system, $\left(\frac{d_2}{d_1}\right)$ is the ratio of outer diameter by inner diameter, L is the length of the system, K is the thermal conductivity of the wall and the insulation (K_{wall} and $K_{insulation}$), A is the cross-sectional area, $T_{Surface}$ is the surface temperature and $T_{Ambient}$ is the ambient temperature.

Heat loss in the overall system without insulation is 1845.45 W and heat loss with insulation is 477.48 W where (overall heat transfer coefficient of air is 22.43 W/m²K, thermal conductivity of pipe is 16 W/m.K, and overall pipe resistance is 0.045 m²K/W). The insulation used in the calculation is ½" thick Alumina Silica Ceramic Fiber which has a thermal conductivity (K) of 0.1 W/m.K.

4.4.3. Dielectric Fluid

All our experiments were run in high viscosity mineral oils (high dielectric strength) in order to provide high insulation between electric components such as diodes and capacitors and to provide high thermal conduction between the heaters (pipe surface) and the capacitors. The other reason for choosing mineral oil is its high stability at high temperatures. It is used in oil-filled transformers, some types of high-voltage capacitors,

etc. Typical specifications of the mineral oil are: auto ignition temperature $\approx$ 300 °C or greater, pour point -30 °C or lower, dielectric breakdown voltage 28 kV/mm (RMS), or greater.

5. CONCLUSIONS AND FUTURE WORK

5.1. Conclusions

Geothermal energy is a renewable resource that can benefit society if it is extracted and used in a cost-effective manner. Based on our research, the concept of integrating a rapid pulsed plasma discharge mechanism into a PDC drill bit offers multiple benefits to the drilling industry: increase in ROP over conventional PDC drilling, decrease in energy requirement, etc.

We presented the design of a bottom hole assembly where the proposed plasma enhanced rock reduction may be used. The whole embodiment is designed within the constraint of the API standards and a downhole form factor. An alternator connected to the mud motor is used to charge a battery bank. The battery bank transfers energy to the inverter and transformer to convert low voltage dc to high voltage ac required by the Cockcroft Walton generator (CWG) circuit. The transformer is connected to a high voltage ac-to-dc rectification and amplification circuit (e.g., the CWG). Between the CWG and the electrode pairs embedded within the drill head/bit, we introduce a distributor head (multiple spark gaps) which will provide appropriate timing for the generation of pulsed plasma discharges at the desired electrode pair, depending on the electrode position spatially on the drill head cross-section.

The BHA form factor design was presented after considering both frictional losses in the pipe and wear due to cavitation at different flowrates. As the diameter of the inner drill pipe decreases the frictional loss in the system increases drastically due to an increase

in velocity. Similarly, the frictional loss in the system increases with the drilling mud flowrate. In contrast to this as the diameter increases the cavitation number also increases due to a decrease in the velocity of the drilling mud. The overall form factor design must optimize the geometry that there is low frictional loss as well as low wear due to cavitation. To show a proof of concept an energy conversion setup (a flow loop setup and an electric energy storage and step-up conversion circuit setup) was built which converts hydraulic energy (flowing water/drilling mud) to high voltage pulses (plasma). The overall efficiency of the energy conversion setup was 37.7%, and this may be improved by increasing the efficiency of the pump and the turbine (or mud motor and alternator in the actual BHA), the latter of which was the least efficient component.

The output of the CWG (100 nF equivalent capacitance) was designed to generate 40 kV pulse which provided 80 J of energy at the rock surface to facilitate crack generation and propagation. The pulse energy may be increased by either increasing the output voltage of the CWG (i.e., by increasing the number of stages in the circuit) or by increasing the capacitance of each capacitor (connecting multiple capacitors in parallel). The frequency of the pulse repetition may be increased by fixing the electrode gap (in the distributor or at the load in water) and by increasing the input voltage. This decreases the charging time of the capacitors and increases the number of discharges per second. Multiple experiments were performed to test the CWG circuit at ambient conditions and a high temperature setup was built to perform experiments at high temperature.

To characterize the CWG circuit and to better understand its operation and limitations (the circuit failed above 25 kV), we modeled the CWG and spark gap switches

73

in a circuit simulator program (LTSpice). This developed model helped in predicting the CWG circuit output at conditions that may not be possible to test experimentally. The analysis showed that the main reason for CWG failure was the surge current experienced by diodes 2, 3, and diode 4 in the two stage CWG which were 240, 7 and 900 A respectively which was higher than the surge rating on the diodes used. High surge current leads to mechanical fractures due to thermal expansion of materials and without proper heat sinking, the diode may go into thermal runaway conditions which will also physically damage the diode and packaging.

Based on the shortcomings we designed a new circuit where each diode is a combination of multiple diodes in series and parallel to achieve appropriate pulse energy ratings based on the current experienced by it. We verified that the discharge time as well as the energy per pulse in the new circuit is not affected by this new design.

5.2. Recommendation for the Future Work

Plasma-aided drilling is applicable for different types of wells (oil/gas, geothermal, etc.) and well depth. The energy to produce the plasma in our design is generated locally, circumventing the need to transfer energy to the bit from the surface. This design also integrates into conventional drill strings without the need to completely replace the drilling setup.

The next steps include producing a prototype for experimental operation where instead of using centrifugal pump and turbine we can use an actual mud motor and alternator to convert hydraulic energy to electrical energy with higher efficiency ($\geq 37\%$). Currently we have characterized the flow setup with water and low viscosity water-based

drilling mud but in future we would need to test different muds such as oil-based mud, synthetic based mud etc. After characterization of the setup, packaging of all the electrical components needs to be investigated so that each component can handle extreme conditions (high temperature$\geq$250°C and high pressure). Testing the technology on different rock formations, downsizing the components to fit into various size drill string diameters also needs to be investigated once the final prototype is complete.

As development for this prototype continues, we are confident the design can become more efficient and adapted to work in various diameter boreholes. This innovation will bring much-needed improvement to the drilling industry, as well as aid in the progress of plasma-based technologies.

REFERENCES

1. Knoema. (2017). BP World Reserve of Fossil Fuels. Retrieved March 23, 2018, from https://knoema.com/infographics/smsfgud/bp-world-reserves-of-fossil-fuels

2. Sawyer, J.S., 1972. Man-made Carbon Dioxide and the "Greenhouse Effect." Nature 239, 23–26. Doi:10.1038/239023a0

3. Bolin, B., 2007. A History of the Sciences and Politics of Climate Change: The Role of the Intergovernmental Panel on Climate Change. Cambridge Univ. Press 1–11.

4. De Moor, A., 2001. Towards a Grand Deal on Subsidies and Climate Change. Nat. Resource. Forum 25, 167–176. Doi:10.1111/j.1477-8947.2001.tb00758.x

5. Walker, G., 1995. Energy, Land Use and Renewables: A Changing Agenda. Land use policy 12, 3–6. Doi:10.1016/0264-8377(95)90069-E

6. National Energy Education Development Project, USA . Infobook. 2012

7. University of Colorado Boulder, Geothermal Energy, Available at website: http://lsa.colorado.edu/essence/texts/geothermal.html [Accessed, 2013-11-04]

8. S.J. Lutz, S. Hickman, N. Davatzes, E. Zemach, P. Drakos, A. Robertson-Tait, Rock mechanical testing and petrologic analysis in support of well stimulation activities at the Desert Peak Geothermal Field, Nevada, in: 35th Workshop on Geothermal Reservoir Engineering, Stanford University, 2010, pp. 335-345.

9. S.J. Lutz, A. Zutshi, A. Robertson-Tait, P. Drakos, E. Zemach, Lithologies, Hydrothermal Alteration, and Rock Mechanical Properties in Wells 15-12 and

BCH-3, Bradys Hot Springs Geothermal Field, Nevada, in: Geothermal Resources Council Annual Meeting (GRC Transactions), Geothermal Resources Council, 2011, pp. 469-476.

10.   T.S. Lowry, J.T. Finger, C.R. Carrigan, A. Foris, M.B. Kennedy, T.F. Corbett, C.A. Doughty, S. Pye, E.L. Sonnenthal, Reservoir Maintenance and Development Task Report for the DOE Geothermal Technologies Office GeoVision Study, SAND2017-9977, Sandia National Laboratories, Albuquerque, New Mexico, 2017.

11.   J.T. Finger, D. Blankenship, Handbook of Best Practices for Geothermal Drilling, SAND2010-6048, Sandia National Laboratories, Albuquerque, New Mexico, 2010.

12.   C. Baujard, R. Hehn, A. Genter, D. Teza, J. Baumgärtner, F. Guinot, A. Martin, S. Steinlechner, Rate of penetration of geothermal wells: a key challenge in hard rocks, in: 42nd Workshop on Geothermal Reservoir Engineering, Stanford University, 2017.

13.   Naganawa, S. (2017). Concept of Thermal-Shock Enhanced Drill Bit for Supercritical Geothermal Drilling. Retrieved from http://pubs.geothermal-library.org/lib/grc/1033738.pdf

14.   Naganawa, S. (2017). Concept of Thermal-Shock Enhanced Drill Bit for Supercritical Geothermal Drilling. Retrieved from http://pubs.geothermal-library.org/lib/grc/1033738.pdf

15. Jamali, & Shahin. (2019). Principle investigation of LaserJet Drilling process and its rock interaction. Retrieved from https://hss-opus.ub.ruhr-uni-bochum.de/opus4/frontdoor/index/index/year/2019/docId/6224

16. Gerlero M., Soroldoni T., Barreto D.: São Francisco Basin Tight Reservoir Play:Defining Benefits of Hammer. Bit/Percussion Drilling, Onshore Brazil. SPE, 2014.

17. Sapińska-Śliwa, Aneta & Wiśniowski, Rafał & Korzec, Michał & Gajdosz, Artur & Sliwa, Tomasz. (2015). Rotary – percussion drilling method – historical review and current possibilities of application. AGH Drilling, Oil, Gas. 32. 313. 10.7494/drill.2015.32.2.313.

18. Plasma Drilling. (2019). Retrieved from https://encyclopedia2.thefreedictionary.com/Plasma+Drilling

19. Tran, J. (2019). Drilling. Retrieved from https://www.studentenergy.org/topics/drilling

20. Vermeij, G. J. Nature: an economic history. (Princeton University Press, 2009).

21. Versluis, M., Schmitz, B., von der Heydt, A. & Lohse, D. How snapping shrimp snap: through cavitating bubbles. Science 289, 2114–2117 (2000).

22. Lohse, D., Schmitz, B. & Versluis, M. Snapping shrimp make flashing bubbles. Nature 413, 477–478 (2001).

23. Tang, X. & Staack, D. Bioinspired mechanical device generates plasma in water via cavitation. Sci. Adv. 5, eaau7765 (2019).

24.   Gavrilov, I. M., Kukhta, V. R., Lopatin, V. V. & Petrov, P. G. Dynamics of prebreakdown phenomena in a uniform field in water. IEEE Trans. Dielectr. Electr. Insul. 1, 496–502 (1994).

25.   Pecha, R. & Gompf, B. Microimplosions: Cavitation collapse and shock wave emission on a nanosecond time scale. Phys. Rev. Lett. 84, 1328–1330 (2000).

26.   Akhatov, I. et al. Collapse and rebound of a laser-induced cavitation bubble. Phys. Fluids 13, 2805–2819 (2001).

27.   Xiao, P. & Staack, D. Microbubble generation by microplasma in water. J. Phys. D. Appl. Phys. 47, 355203 (2014).

28.   G. Hanington, "Using Parallel High-Voltage Multipliers for 100 kV Downhole Neutron Generator Power Supplies," International Conference on High-Temperature Electronics, May 13-15, 2014, pp. 6-12. Doi: 10.4071/HITEC-TA12.

29.   Dwivedi, C. and M. Daigvane. Multi-purpose Low Cost DC High Voltage Generator (60 kV Output), Using Cockcroft-Walton Voltage Multiplier Circuit. In Emerging Trends in Engineering and Technology (ICETET), 2010 3rd International Conference on. 2010. IEEE.

30.   Brugler, J., Theoretical performance of voltage multiplier circuits. Solid-State Circuits, IEEE Journal of, 1971. 6(3): p. 132-135.

31.   J. D. Cockcroft and E. T. S. Walton, Proc. R. Soc. London 136(830), 619 (1932).

32.   G. Henneberke, Nucl. Instrum. Methods 7(1), 89 (1960).

33.   L. L. Reginato and B. H. Smith, IEEE Trans. Nucl. Sci. 12(3), 274 (1965).

34.   E. Hara, Nucl. Instrum. Methods 54(1), 91 (1967).

35. Joseph MB (2001). Using rectifiers in voltage multipliers circuits. General Semiconductor. Retrieved from www.eettaiwan.com/ARTICLES /.../2001J UN14_AMD_AN2009.PDF General Semiconductor.

36. Spencer DFR (2001). Aryaeinejad and E.L. Reber. Using the CockcroftWalton Voltage Multiplier Design in Handheld Devices. Idaho National Engineering and Environmental Laboratory, P.O. Box 1625, Idaho Falls, ID 83415.

37. High temperature & High pressure alternators for oil and gas exploration (2019). Retrieved from https://www.ducommun.com/pdf/hightempaltern.pdf

38. Sharewell | Charger Industries. (2019). Retrieved from http://chargerind.com /product/sharewell/

39. A Very High-Temperature Inverter for Energy Storage Applications Utilizing Silicon-on-Insulator and Silicon Carbide Electronics. (2005). Retrieved Arkansas Power Electronics International, Inc. Retrieved from https://www.sandia.gov/ess-ssl/docs/pr_conferences/2005/Schupbach.pdf.

40. 10 kV Neon Sign Transformer kit (2019) Retrieved from https://www.amazon.com/10kv-Neon-Sign-Transformer-Kit/dp/B0083UK8LU /ref=sr_1_43?crid=1BF4T9PX1JY37&keywords=neon+sign+transformer&qid= 1575336454&sprefix=neon+sign+%2Caps%2C797&sr=8-43

41. Edoardo Rossia, Shahin Jamalic, Volker Wittigc, Martin O. Saarb, Philipp Rudolf von Rohra, "A combined thermo-mechanical drilling technology for deep geothermal and hard rock reservoirs", Geothermics 85 (2020) 101771, https://doi.org/10.1016/j.geothermics.2019.101771

42. K. G. Pierce, B. J. Livesay, J. T. Finger, "Advanced Drilling Systems Study", SAND95-033 1 Unlimited Release Printed June 1996, https://prod-ng.sandia.gov/techlib-noauth/access-control.cgi/1995/950331.pdf

43. United Nations Secretary-General Ban Ki- moon, United Nations https://www.un.org/sustainabledevelopment/blog/2015/12/un-chief-offers-thanks-to-civil-society-for-its-role-in-paris-agreement/

44. M. Voigt, E. Anders, F. Lehmann, "Electric Impulse Technology: Less Energy, Less Drilling Time, Less Round Trips", SPE Asia pacific oil and gas conference and exhibition, Perth, Australia, 25-27 Oct 2016, SPE-182197-MS

45. Zehao LyuXianzhi SongGensheng LiYu ShiRui ZhengGaosheng WangYu Liu, "Investigations on thermal spallation drilling performance using the specific energy method", Journal of Natural Gas Science and Engineering, Volume 54, June 2018, Pages 216-223

46. Akhter, M., Mallams, J., Tang, X., Kazi, A., Kao, Y.-T., Kumar, S., Tai, B., Antao, D., Palazollo, A., and Staack, D.: 2019, APS Annual Gaseous Electronics Meeting , Texas A&M University, Aug 2019.

47. NOAA (National Centers for Environmental Information), 2015

48. Iti Harshad Patel, Optimal Heat Extraction for Geothermal Energy Applications, Thesis, 2016

49. Retrieved from US Energy Information Administration, Monthly energy review, Table 1.3, April 2018

50. Retrieved from http://lsa.colorado.edu/essence/texts/geothermal.html#:~ :text= Heat%20is%20continuously%20produced%20within,partly%20rock%20and%20 partly%20magma.

51. Goldstein, B., Hiriart, G., Bertani, R., Bromley, C.J., Gutierrez-Negrin, L., Huenges, E., Muroaka, M.A., Ragnarsson, H., Tester, J., 2011. Geothermal Energy, in: Zemedkun, M.T., Wratt, D. (Eds.), IPCC Special Report on Renewable Energy Sources and Climate Change Mitigation. Cambridge University Press, Cambridge, UK and New York, NY, USA, pp. 401–436.

52. Retrieved from http://www.spring8.or.jp/en/news_publications /research_ highlights/no_57/

53. Retrieved from drillingcontractor.org

54. Retrieved from slb.com/Impax

55. Retrieved from https://www.solar-electric.com/learning-center/deep-cycle-battery-faq.html/

56. Retrieved from https://theinverterstore.com/product/2000-watt-48-volt-rack-mount-inverter-to-120-vac-pure-sine/

57. Retrieved from https://www.electricaleasy.com/2014/04/transformer-losses-and-efficiency.html#:~:text=Efficiency%20of%20Transformer&text=Transformers% 20are%20the%20most%20highly,between%2095%25%20to%2098.5%25%20.

58. Lezhenin, F. F., & Gnesin, G. G. (1967). Thermal conductivity of silicon carbide at high temperatures. Powder Metallurgy and Metal Ceramics, 6(2), 114-116. Retrieved 11 19, 2020, from ttps://link.springer.com/article/10.1007/bf00775642

59. Retrieved from https://www.bluedemon.com/Pg7-DRILLROD1.HTM

60. Retrieved from https://www.bsee.gov/sites/bsee.gov/files/tap-technical-assessment-program//013ac.pdf

61. Li, Zifeng. (2014). Criteria for jet cavitation and cavitation jet drilling. International Journal of Rock Mechanics and Mining Sciences. 71. 204–207. 10.1016/j.ijrmms.2014.03.021.

62. Retrieved from https://www.analog.com/en/design-center/design-tools-and-calculators/ltspice-simulator.html

63. Kazi, Aamer & Riyaz, Mirza & Tang, Xin & Staack, David & Tai, Bruce. (2020). Specific cutting energy reduction of granite using plasma treatment: A feasibility study for future geothermal drilling. Procedia Manufacturing. 48. 514-519. 10.1016/j.promfg.2020.05.077.

64. Retrieved from https://en.wikipedia.org/wiki/Voltage_multiplier #Dickson _charge_pump

APPENDIX A

DRILLING MUD

Drilling Mud Selection

Drilling mud is a heavy, viscous fluid mixture that is used in oil and gas/geothermal drilling operations to carry rock cuttings to the surface and also to lubricate and cool the drill bit. The drilling mud, by hydrostatic pressure, also helps prevent the collapse of unstable strata into the borehole and the intrusion of water from water-bearing strata that may be encountered. We intentionally designed and fabricated our hydraulic/flow-to-electrical energy conversion test setup from stainless steel material (piping, valves, pump, *etc.*) so as to enable higher temperature and aqueous/non-aqueous fluids operational capabilities. We have shortlisted oil-based drilling fluids for our testing since they have better fluid loss control, shale stability, faster penetration rates, and they are designed to handle high temperature and pressure conditions. The oil-based mud will primarily contain diesel with chemicals such as barite, lime, safe-carb, calcium chloride, etc. (please refer to Table A-2).

The major functions of a drilling fluid include;

1. Improving the hydrostatic pressure while drilling so as to eliminate formation fluids from finding their way back into the wellbore.

2. Cools, cleans, and supports the drill bit and its assembly during drilling.

3. Prevents damage to the formation and avoiding the corrosion of drill pipes.

4. Pushes out and suspends drill cuttings (debris of rock materials and mud) during drilling.

5. Minimizes environmental impacts and hazards resulting from drilling.

Classification of Drilling Fluids

Major Classification

1. **Water-Based Mud (WBM)**

   This is a class of drilling fluid that has fresh or seawater as its continuous phase. Its composition includes mixtures of aqueous polymers, clay, and brine. It is the most predominant type of drilling fluid.

2. **Oil-Based Mud (OBM)**

   This class of drilling fluids has oil (usually gas oil) as its continuous phase, an average molecular weight of about 120 to 1000 and is synthesized from one or more olefin monomers with a carbon chain of about C_2 to C_{14}. Although OBM is amongst the less used drilling fluids today because of their expensive nature, they also guarantee better results when used.

3. **Synthetic Based Mud (SBM)**

   This category of drilling mud is quite similar to the OBM but less harmful in terms of its toxicity and environmental impact. They are mainly composed of olefins, esters, and sometimes paraffins. In terms of its application, SBM has a low kinetic viscosity and thus could be used under low-pressure conditions

Minor Classification

4. **Emulsion Drilling Mud (EDM)**

5. **Invert Emulsion Mud (IEM)**

6. **Air Drilling Fluid**

7. **Foam Drilling Fluids**

Properties of Drilling Fluids

In a typical geothermal drilling operation, the flow rate typically ranges from 100 to 1000 GPM, the density ranges from 9 to 21 pounds per gallon (1078 to 2516 kg/m^3) and the plastic viscosity ranges from 11 to 25 cP.

a) **Rheology:** This is a property of fluid that talks about viscosity. A high viscous fluid may be able to carry drill cuttings to the surface freely alongside other weighting agents in the mud.

b) **Density:** Requires enough hydrostatic pressure to avoid the drilled borehole from caving in, thereby keeping the formation fluid from entering the borehole. Drill muds with high density than the cuttings density makes cleaning of wellbore easier and faster.

c) **Fluid Circulation Loss:** A good drilling fluid should be able to have a low permeability effect so as to be able to seal the pores between the formation and wellbore.

d) **Solid Content:** Solids could be high gravity (HGS) e.g. barite and other weighting materials or low gravity (LGS) e.g. clays, polymers, and bridging materials. Drilling fluids with high solid contents (i.e. LGS) usually increase plastic viscosity and gel strength because they have more thicker filter cakes and slow drilling rates than low solid content fluids (i.e. HGS).

e) **Chemical Properties:** This is a major property of drilling fluids that affects performance and wellbore stability. It monitors salt formations, pH and corrosion effects of a drilling fluid.

Flow rate of Drilling Mud

Flow rate of a drilling mud depends on a lot of factors such as:

- Cuttings specific gravity

- Drilling fluid viscosity

- Drilling fluid density

- Annulus OD

- Annulus ID

- Rate of penetration

- Rotary speed

- Cuttings concentration

- Depth

Components of Water-Based Drilling Fluid

Table A-1 Chemical composition of water-based drilling mud

Sample type	Product	Weight (Grams)
Water-Based mud	Water	291.4
	M-I Bar	25
	Versa Trol	1
	Soda ash	1
	Versa Mul	1.5
	Versa Mod	10.5
	Caco3 (M)	15
	Versa gel HT	4
	LVT-200	93

Chemical composition of water-based drilling mud is shown in Table A-1. M-I Bar barite is a high-quality drilling-grade barite (barium sulfate) used to increase the density of drilling fluids. Versatrol resin is a naturally occurring asphalt used for HPHT filtration control in oil-based muds and is often used to seal low-pressure and depleted formations. Soda Ash, another term for sodium carbonate. It is used to treat most types of calcium ion contamination in freshwater and seawater muds. Versamul package forms the basic brine-in-oil emulsion required. Versamod packages enhance emulsion

characteristics and lower fluid loss and increase viscosity. Calcium Carbonate, CaCO3. It is an acid-soluble weighting or bridging agent for use in drilling. Versagel HT clay is an effective viscosifier in oil and water-based drilling fluid systems and is temperature stable to 400 °F (204 °C). This viscosifier is unaffected by contaminants normally encountered in drilling and contributes to the HTHP fluid loss of the system. LVT 200 is used as a low viscosity base oil for the formulation of Petro Drill systems. It is also used as a base oil for spotting fluids in water-based drilling fluids. Occasionally LVT 200 is used in the water-based drilling fluid to improve lubricity.

Components of oil-based drilling fluid

Table A-2 Chemical composition of oil-based drilling mud

Sample type	Product	Weight (Grams)
Oil Based mud	Oil	155.7
	Safe carb	15
	Lvt-200	27
	Mul XT	5
	Barite	56
	One-Trol Ht	3
	Lime	8
	Surewet	19
	Cacl2	22.37
	Cc-555	1

Oil is a petroleum product such as diesel fuel. Safe Carb ground marble is a high-purity, acid-soluble, calcium carbonate used as a bridging and weighting agent in drilling. Mul XT emulsifier is used as the primary emulsifier in all systems to provide low viscosity stable emulsions and excellent oil wetting at extreme temperatures. Barite heavyweight additive is a barium sulfate material used to weight drilling muds and cement slurries. One-Trol HT additive can be used in any oil- or synthetic-based drilling fluid system to control fluid loss. Lime, common term for calcium hydroxide. It is used as a stabilizing ingredient in oil- and synthetic-base mud, essential to the formation of fatty-acid soap emulsifiers. Surewet system surfactant preferentially wets barite and drill solids to prevent water-wetting of solids. Secondary functions include improving thermal stability, rheological stability. Calcium Chloride is used in drilling mud to cool and lubricate the bit and to remove cuttings from the hole. $CaCl_2$ helps add density to the mud to overcome formation pressures and keep oil, gas, and water in place.

APPENDIX B

THERMOCOUPLE CALIBRATION

We calibrated thermocouples to enable accurate temperature measurement in our test setup. We used LabVIEW to acquire temperature data. T-type thermocouples are calibrated against the pre-calibrated RTD (NIST). All the thermocouples and RTD were put inside the oven and kept at a distance so that one thermocouple can not effect the reading on others.
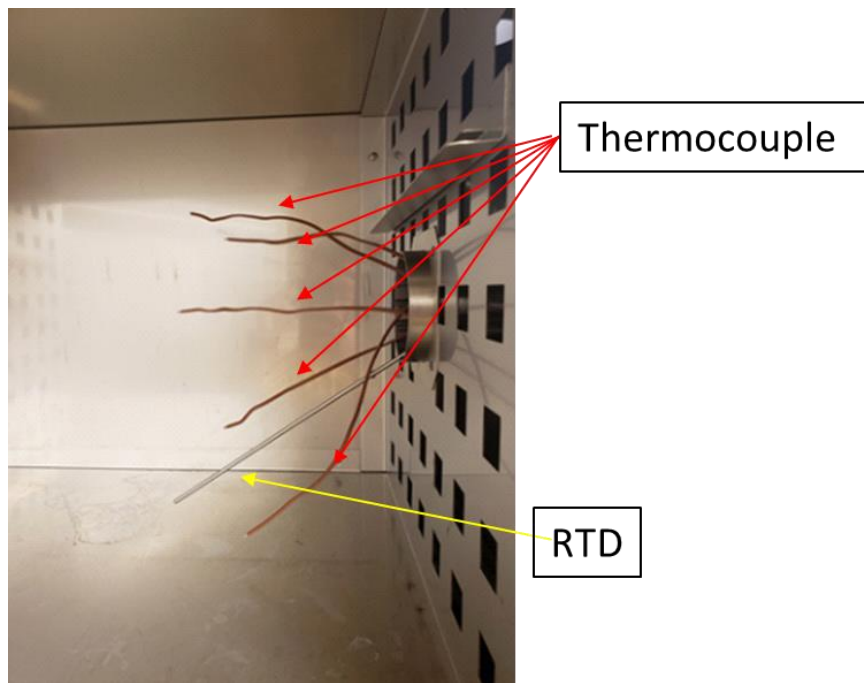
Figure B-1 Thermocouple and RTD placement inside the oven for high-temperature calibration

We connected the thermocouples to NI DAQ 9171 and RTD to NI DAQ 9174. Both T type thermocouples and RTD are inserted into the oven for high-temperature calibration(30-300°C) (Figure B-1). After this oven was switched on and once the temperature became stable, we started collecting the data using LabVIEW. Temperature of the oven was kept on increasing by 10°C and data was collected till 240°C. We plotted the graph for "time vs temperature" for each temperature in MATLAB to get the slope and intercept of both the thermocouple and RTD. Once we got the data, we fit the slope and intercept of thermocouple according to RTD so that both of them became equal as shown in Figure B-2.

Magnified image

Figure B-2 Recorded temperature vs Calibrated temperature for different thermocouples and RTD

APPENDIX C

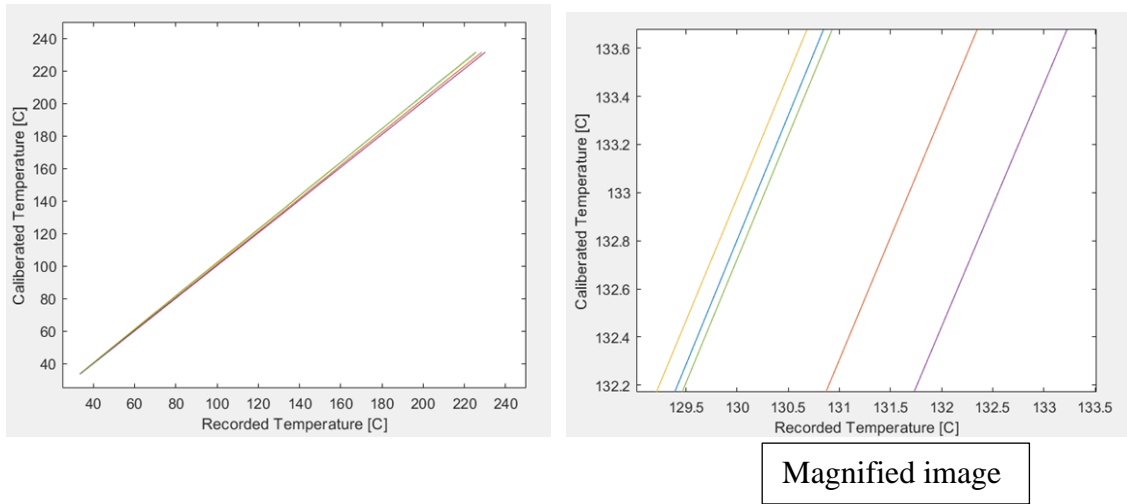HIGH PRESSURE CHAMBER

We designed a high-pressure vessel to perform cutting (non-assisted and shockwave/plasma assisted) at geothermal conditions of high pressure and temperature. The vessel is a five sided studded API cross with a bore-hole of diameter ≈2.56". Additionally, the sixth side of the cross is a blind hole of depth 2" (diameter ≈2.56") to house the test sample (*i.e.*, a rock) and the test sample fixture/holder. Figure C-1(a) shows a three-dimensional (3D) model of the studded-cross pressure vessel, Figure C-1(c) shows the real model of the studded cross and Figure C-1(b) shows a two-dimensional (2D) sectional view with the relevant dimensions. The top face (side 5) of the studded cross will house a high pressure and high temperature rotary seal to enable externally-driven rotary motion of the cutting shaft. The flanges on two opposite sides (labeled, side 1 and side 2 in Figure C-1(d)) will house viewports to facilitate imaging and lighting of the processes (cutting and plasma discharges) occurring inside the pressure vessel. Flanges on the other two sides (labeled, side 3 and side 4 in Figure C-1(d)) will house feedthroughs (fluid, temperature, electrical- high and low voltage, etc.), pressure gauges, and a pressure relief valve. Heating of the pressure vessel will be both externally via ceramic heaters, and internally (locally near the rock test sample) using rope and cartridge type heaters. The pressure vessel will be capable of pressures ≈10 ksi and temperatures ≈250 °C.
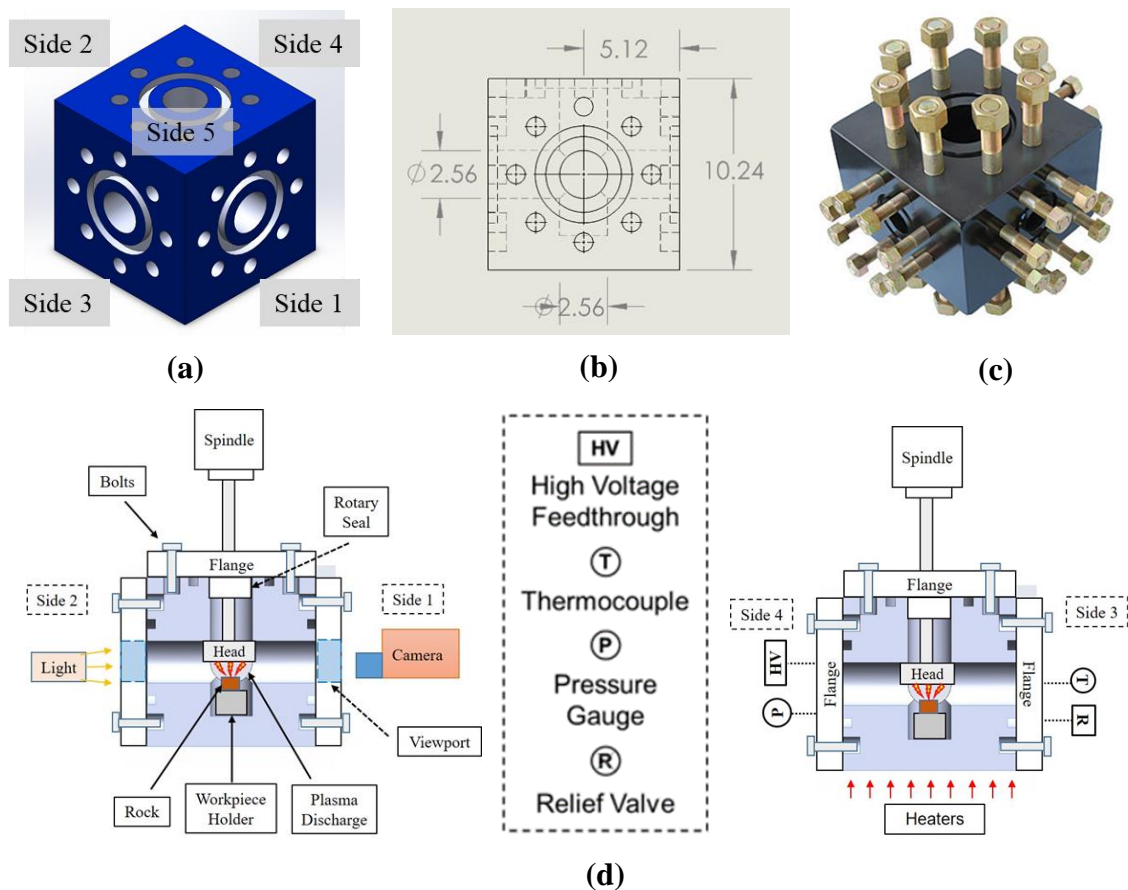
Figure C-1 High pressure test orthogonal cutting test setup: (a) 3D model of the five-sided studded cross pressure vessel with dimensions for ≈10 ksi pressure rating shown in the 2D sectional view in (b). The image in (c) is an actual six sided studded cross. The schematics in (d) show the pressure vessel with the major components

Figure C-2(a) shows a detailed sectional CAD model of the pressure vessel showing the major internal components. The pressure vessel consists of different components such as shaft, retention plate, fly cutter, fixture, rotary seal, and bushing. The shaft is attached to the CNC spindle on one end and a fly cutter on the other to house the polycrystalline diamond (PCD) inserts. A retention plate which is shown in Figure C-2(b) will be placed inside the studded cross which houses the high pressure rotary seal

(provides a seal for the rotating shaft) and a bronze bushing (to provide structural support for the shaft and minimize deflection). The retention plate also consist of two threaded holes at the top surface to safely remove the plate from the studded cross once the experiment is done, two blind holes for anti rotation pins to prevent movement of the plate and an o-ring groove along the plate circumference to accommodate an o-ring which will serve as a static seal between the high and low pressure region. The o-ring and the o-ring groove has been designed as per ASTM standard (AS568B) and is listed in . Based on the ASTM standards parameters, we selected the AS568-143 o-ring and we chose the material to be Viton® fluoroelastomer for its high temperature and chemical resistance capabilities. The top face flange for side 5 of the studded cross (Figure C-2(c)) has a 0.5" concentric hole for the shaft and two 0.05" blind holes for anti-rotation pins. Figure C-2(d) shows the CAD model of the flange for side 1 which will be used for the following instrumentation: a pressure gauge with the cooling element, a high voltage electrical feedthrough, a rupture disc rated for 10 ksi, and a variable pressure relief valve (1-10 ksi). The rupture disc and pressure relief valve will act as safety relief mechanisms in case of emergency events where the pressure exceeds the safety limit. Figure C-2(e) shows the CAD model of the flange for side 2 which will house the following instrumentation: three 1/8" NPT-to-tube compression fittings for thermocouple probes (temperature measurements), two 0.25" NPT-to-tube compression fittings for water inlet and outlet tubes, and one 0.5" NPT power feedthrough for internal power requirements (e.g., the heaters). In addition to the internal instrumentation, fiberglass rope heaters will also be used to heat the outer surfaces of the studded cross which will enable experiments in the temperature range of 20-250 °C.
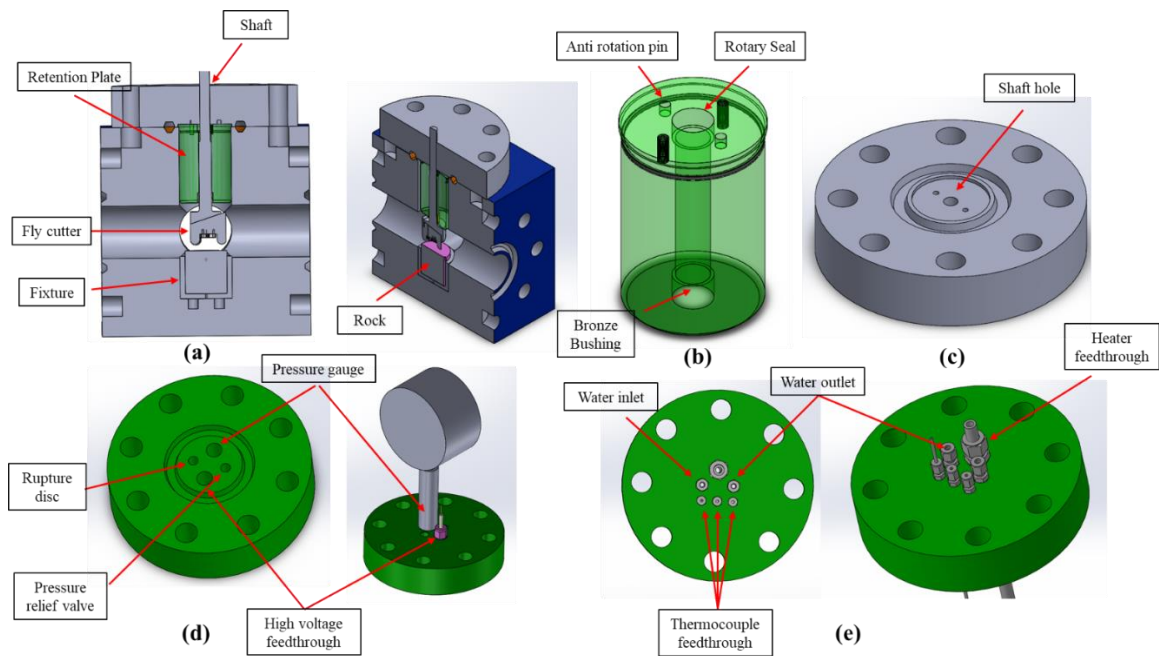
95

Figure C-2 High pressure orthogonal cutting test components: (a) Sectional view of the high pressure test setup with internal components. The CAD model of the retention plate with rotary seal, bushing and O-ring groove (b). The CAD model of the top flange (c). CAD model of the side flange 2 and 3 with the instrumentation is shown in (d) and (e) respectively

Table C-1 O-ring and the O-ring groove dimensions for different parts

Part no	Inner Dia	Outer Dia	Cross section	Groove depth	Compression	Groove width
143	2.425''	2.631''	0.103''	2.4745''	0.42 (42.7%)	0.1545''
229	2.359''	2.637''	0.139''	2.407''	0.44 (44%)	0.2085''
331	2.225''	2.645''	0.21''	2.270''	0.31 (31%)	0.315''

In order to hold the rock sample in place, a work piece holder was also designed as shown in Figure C-3(a). The rock sample will be held in place with the help of keyway slots and set screws. The hole at the bottom is a provision to push the sample out in case the need of an adhesive is identified. The legs of the holder will fit into complementary blind holes machined into the bottom of the studded cross sixth-side blind hole to prevent rotation of the work piece holder. We performed a static finite element analysis to estimate the effect of rock cutting force and weight on bit on the stress, strain and deformation of the rock holder (Figure C-3(c),(d)). In the simulation we put a force of 3000N on the base surface and 1000N each on the legs of the holder (Figure C-3(b)). A maximum stress of 73MPa and maximum deformation of 3.3 μm is found at the center of the rock holder which we consider to be minimal for the material chosen, i.e., low carbon steel with a yield strength of 370 MPa (factory of safety ≈5). Our pressure vessel (5-sided studded cross) and all other major components are being sourced from local US-based vendors and manufacturers.

Keyway slots

Set screws slots

Fixed

3000N

1000N

1000N

(a)

(b)

Cartridge
heaters slot

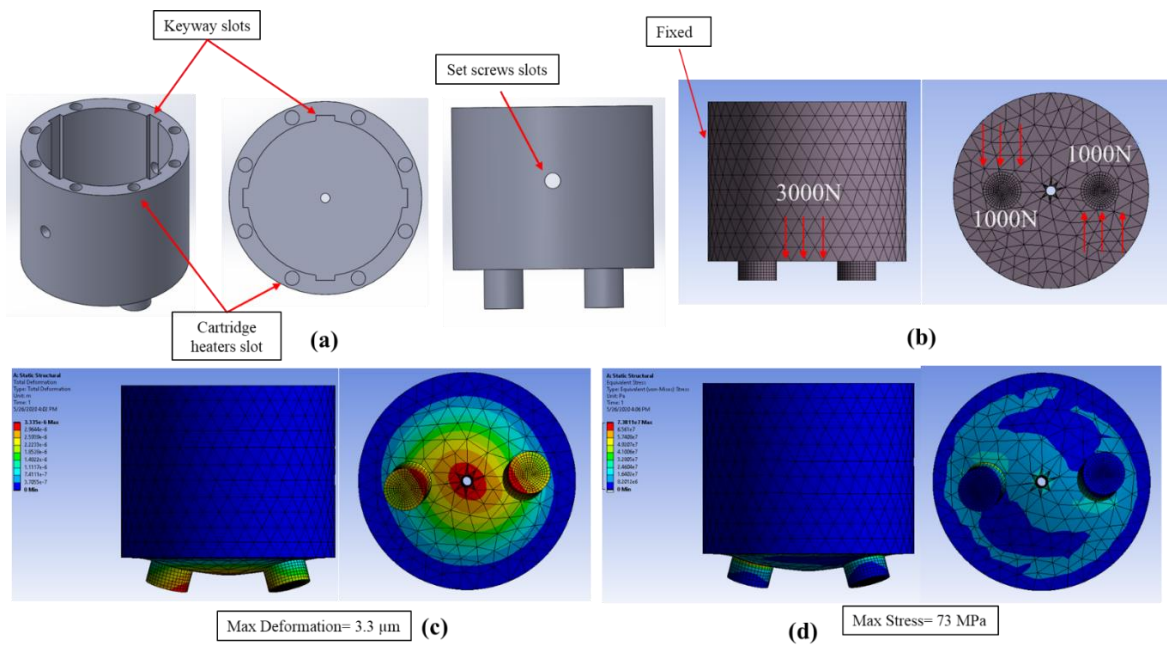Max Deformation= 3.3 μm **(c)**

(d) Max Stress= 73 MPa

Figure C-3 Workpiece holder design: CAD model of workpiece holder on different planes (a). The force applied on different faces of the workpiece holder is shown in (b). Deformation and Maximum stress results of the holder is shown in (c) and (d) respectively